



A nodal-based optimization method for the design of continuous fiber-reinforced structures

Xuyu Zhang^a, Yi Min Xie^a, Qing Li^b, Cong Wang^a, Zicheng Zhuang^c, He Li^a, Shiwei Zhou^{a,*}

^a Centre for Innovative Structures and Materials, School of Engineering, RMIT University, GPO Box 2476, Melbourne 3001, Australia

^b School of Aerospace, Mechanical and Mechatronic Engineering, The University of Sydney, Sydney, NSW 2006, Australia

^c Department of Building and Real Estate, The Hong Kong Polytechnic University, Hong Kong, China

ARTICLE INFO

Keywords:

Fiber path optimization
Fiber-reinforced composite
Variable stiffness composite
Nodal-based evolutionary optimization

ABSTRACT

The mechanical performance of fiber-reinforced structures highly relies on fibers' paths in the matrix material. Unlike the level set method that offsets the zero-level contours of a higher-dimensional function, this work shifts the nodes of a truss network within an optimization framework to design individual paths specifically. All intersection manners of a single fiber with the rectangular continuum element are considered in the finite analysis to retrieve mechanical responses within an acceptable error margin numerically. The design variables, namely node coordinates, are updated via the method of moving asymptotes under the guide of the sensitivity of the objective function, which is smoothed using a radial basis function. After each optimization iteration, the paths are slightly adjusted to avoid twisting problems and control fiber gaps using a polynomial interpolation scheme. Numerical examples illustrate that the proposed method can generate elegant fiber paths within a few steps. In the meantime, the optimization efficiency is improved as the design variables are significantly reduced. Compared with existing methods, we found that lower objective values can be achieved as allowing nodes to move freely in the design domain guarantees a global minimum theoretically.

1. Introduction

Fiber-reinforced structures, the mixture of the matrix phase and short/continuous fibers [1,2], have been widely used in aviation, aerospace, marine, automation, civil infrastructures, and medical instruments [3–5] due to their high stiffness, super strength-to-weight ratio, excellent fatigue, and fantastic corrosion resistance performance. In addition to the constituent materials, the fiber layout plays a crucial role in their performance. For instance, curved fiber paths can provide continuous-discrete variable stiffness composites (VSC) [6,7] with better mechanical properties than the constant-stiffness composite [8]. It was reported that the tensile stress of a fiber-reinforced structure could be improved by 36% if its originally straight-shaped curves flow around its central cavity [9]. Experiments also show that the fibers parallel with principal stress increase the structural stiffness and improve the post-buckling properties without increasing the weight compared to conventional quasi-isotropic fiber structures [10–12]. Therefore, it has great potential to improve the mechanical properties of fiber-reinforced structures.

Researchers have found that fibers' direction, volume content, and

layup sequence can be well designed to improve stiffness, strength, elasticity, and anisotropic properties [13]. Several pioneering works calculated principal stresses [14] or strains [15–17] of fiber-reinforced structures using orthotropic material properties in finite element analysis and made the optimal fibers parallel with one of them. The stress-based approach appears to produce slightly more efficient structures than the strain method due to the lower sensitivity of the stress field to changes in fiber orientation [18,19]. However, since compliance is nonconvex in fiber angle variation, the optimization problem has multiple local minima. Furthermore, the potential duplicate global minima made it impossible to find a unique fiber layout under certain conditions. Luo et al. proposed the energy method [20] to correct these defects, in which the displacements are assumed to be continuous across the adjacent elements after a change in element orientation. The stress and strain of each element are different across the adjacent elements, and the energy method introduces additional stress and strain at the interface location to eliminate discontinuity. However, the optimal orientation of the fiber is low in continuity, and the fiber angle changes significantly in each iteration [21]. Moreover, the energy method is challenging to apply to the 3D optimization problem [22].

* Corresponding author.

E-mail address: shiwei.zhou@rmit.edu.au (S. Zhou).

<https://doi.org/10.1016/j.compstruct.2023.117455>

Received 14 May 2023; Received in revised form 19 July 2023; Accepted 14 August 2023

Available online 14 August 2023

0263-8223/© 2023 The Authors. Published by Elsevier Ltd. This is an open access article under the CC BY license (<http://creativecommons.org/licenses/by/4.0/>).

Direct material optimization approach [23,24], shape function and penalty method [25], and binary coding parameterization method [26] can avoid local minima by considering fiber orientations in the effective elemental stiffness. The direct material optimization method employs an effective stiffness using a weighted sum of several fiber orientations. Subsequently, the optimization objective was to drive a single weight to one while the other weights approach zero so that only a single material (fiber orientation) is selected for each element [24]. The virtual quasi-isotropic composite structure is applied as the initial structure. Therefore, these methods depend less on the initial solution than those directly optimizing the fiber orientation [23,24]. The direct material optimization method assumes a fiber with a distinct orientation (e.g., 0° , $\pm 45^\circ$, 90°) as a unique material to reduce design variables [24]. Two other discrete fiber angle optimization methods [25,26] use weighted formulas to parameterize different fiber orientations and reduce the number of design variables required for a finite selection of fiber orientations. However, these fiber-orientation-based methods render discontinuous fiber, including abruptly-changed fiber angles [20]. These defects will likely result in stress concentration and manufacturing difficulties [27].

Fiber-reinforced composite design using structural topology optimization methods has become a new trend in this field [28–30]. Density-based topology optimization methods [31] were used for pioneering works due to their simplicity and ease of use. Unlike the isotropic material model used in traditional structural topology optimization for single-phase structures [32,33], material orthotropic was considered in fiber optimization by adding fiber angles as design variables [21]. In a related study, this method combined with a dynamical system [34] was conducted for the composite design, resulting in structures 66–90% lighter than the initial conditions. Similarly, this approach has been successfully extended to the design of 3D composites, and relevant parts have been produced with additive manufacturing based on the optimized design [35], improving the stiffness of parts by 14–29%. Moreover, a bi-material-density-based topology optimization framework is developed for length scale separation and the decreased design freedom problems by considering the total volume and local fiber proportion constraints to generate continuous fiber paths [13].

Smooth fibers can be naturally and implicitly expressed as the zero-level contour of a higher-dimensional level set function [36,37]. With such a novel expression method, the continuously varying fiber paths can be optimized by the level-set method with the analytical sensitivity of energy-based approximation [38], reducing compliance by up to 86%. Further, the level set method was utilized with the offset method for material distribution and fiber path optimization of additive manufacturing composites, which had advantages over other methods in complex cases such as L-shaped brackets [21]. However, the initial condition often influences the optimization results of the level-set method. Fiber optimization will have more design flexibility if the level set function is parametrized by a set of radial basis functions since RBFs are only spatial coordinate-related, and the evolution process is transformed to update the coefficients [39]. In a similar work, fiber paths were designed by parameterizing their orientations with a nodal level-set function, reducing mean compliance by at least 50% [40].

The bi-direction evolutionary structural optimization (BESO) method [41] has also been introduced into the fiber-reinforced composite design. An early pioneering study extended the BESO method from isotropic materials to anisotropic composites [42], reducing compliance by 50%. In follow-up studies, the BESO method was used for multi-scale optimization problems of porous materials [43,44], which can be analogous to the fiber orientation problem. Likewise, a two-scale topology optimization method to concurrently optimize the general topology of structure and the material orientation based on the BESO method, where an analytical approach with the hybrid stress-strain method is adopted to determine the optimal material orientation, obtaining a 50% reduction in compliance [22]. In addition, an anisotropic topology optimization based on the BESO algorithm for designing

composite parts [45] optimized both the part shape and the local fiber orientation, directly obtaining the part structure manufactured by fiber placement technologies.

Automatic fiber placement and additive manufacturing allow the fabrication of composite structures with continuous but spatially varying fiber. Thus, it is highly demanded to consider their fabrication features in optimization design. In the related work, a force line approach is proposed to place fiber-reinforced filaments along the load paths to design parts for additive manufacturing [46], achieving higher strength and toughness. However, the design of VSC should satisfy several manufacturing constraints, such as the fiber continuity, the minimum gap requirement, and the minimum turning radius of fiber paths [7,47]. Although intersected fibers may facilitate load transfer under limited circumstances (e.g., in woven- or knitted-fiber composites [48]), overlapped fibers fabricated by AFP or additive manufacturing lead to undesired thickness variations [49,50]. Furthermore, some experiments and simulations have shown that fiber knots can significantly reduce structural performance and might result in material failure [51,52]. Therefore, it is crucial to comply with manufacturing constraints during the design phase to avoid structural defects. In addition, the fiber paths must be defined as smooth continuous curves to be manufacturable by automatic fiber placement or 3D printing. A sharp turn of the fiber orientation angle may cause structural defects, including buckling or stress concentration, leading to reductions in structural performance [53]. Moreover, the material properties of composites with discontinuous fibers, such as strength or stiffness, are lower than those with continuous fiber paths, as short fiber or particle structures are mechanically inferior to continuous fiber structures [54]. Therefore, it is necessary to take manufacturing constraints into account in the optimization problem.

The critical issue in optimizing fiber paths is ensuring fiber continuity and avoiding fiber crossover, specifically truss intersections (as described in detail below). One solution to this problem is to express the fiber path as a curve function. This parameterization forces continuity and smoothness of the fibers and reduces optimization variables [55]. In the initial research, Gürdal et al. studied linearly changing fiber directions widely used in designing variable stiffness plates [56]. After that, quadratic functions, cubic functions [57], and trigonometric functions [58] were introduced to describe the path of the fiber. However, this kind of function path is relatively simple, and the complexity is insufficient. In order to expand the shape of the fiber path that can be designed, more complex functions are also applied, including Bezier curves [59] and Lagrange polynomials [60,61]. The flow field function has described the fiber path arrangement of variable stiffness composite plates [62]. In their research, the flow field function consists of a uniform linear flow field and a two-point vortex based on the superposition theorem. Although this type of processing limits the design space of advanced manufacturing technologies, it provides direct access to smooth fiber trajectories, which gives us great inspiration.

Recently, feature-mapping methods that predetermine fiber orientation in each primitive before optimizing its layout have gained significant attention. Based on the movable morphable component method that utilizes exclusively geometric primitives [63], Sun et al. proposed an explicit topology optimization method for fiber-reinforced materials to effectively optimize the structural layout and fiber orientation angle while considering the specified number of fiber layers and layer thickness [64]. The geometry projection method [65,66] capable of generating composed primitives was expanded by Smith and Norato to design orthotropic fiber-reinforced bars via projecting the structure onto a fixed finite element mesh for analysis and adjusting bar node position [67]. Though this method works on the design of spatial composite laminates and VSC [68], it is primarily used for structures composed of unidirectional fiber-reinforced bars or laminates.

It can be seen from the above literature review that fiber path optimization is still an open topic at present. However, these existing methods have some drawbacks. The first type of scheme defines the fiber

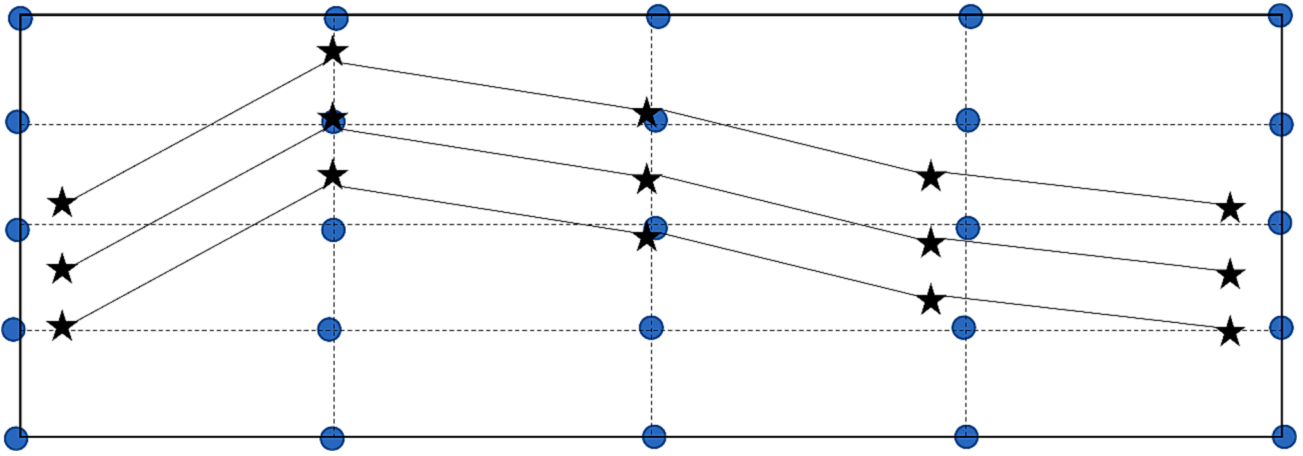


Fig. 1. An example of VSC with 4×4 rectangular elements and three continuous fibers. Black star points represent nodes of the continuum elements. The blue points represent nodes of the truss elements.

orientation of the element center or design point as a design variable [27,69]. This scheme provides a more extensive design space but requires post-processing to extract fiber paths and has difficulty in satisfying manufacturing constraints. Second, the analytic function defines the fiber path [57–61]. These methods guarantee the bent fibers' continuity and significantly reduce the design variables. However, the quality of the optimized design depends heavily on the type of analytical function. Third, in the level set-based method, the contours of the scalar function are used to describe the curve fibers [38,39]. These methods do not require post-processing to extract fiber paths and naturally avoid fiber crossings. However, the level set-based fiber optimization procedure requires many iterations and a complex derivation of the sensitivity. Moreover, this method still treats composite as an orthotropic material in the finite element analysis ignoring the effect of fiber density on the mechanical properties.

Fiber-reinforced constructions can be continuous or short fiber-reinforced structures. However, this work only focuses on continuous fiber design in automatic fiber placement and additive manufacturing. Given the above reviews and facts, this work proposes a node position-based fiber path optimization method for VSC design. To the best of our knowledge, no studies on topology optimization methods for FRC employ node coordinates as design variables. Compared with the optimization method using the elemental orientation as the design variable, the proposed method is more intuitive for obtaining the fiber paths directly and sets moving limits to meet manufacturing constraints. Compared to the level-set method, the proposed method is more straightforward in sensitivity derivation, and the structure of each fiber is obtained based on rigorous mechanical analysis. Nodal position-based optimization methods have optimized discrete structures [70–72], where the researchers used the nodal coordinates of discrete elements as design variables to optimize the structural stiffness by updating the nodal coordinates and connection methods. Resembles the geometry projection method mentioned for fiber-reinforced composites [67], treating rebars as embedded discrete elements and manipulating their endpoints can lay out the reinforcement to minimize weight or compliance [73]. Inspired by this concept, we express fibers embedded in the matrix material as a continuous truss network and control its nodes to yield desirable fiber paths. In addition, the endpoints would be fitted by polynomial functions and corrected according to the fitted functions. Finally, the overlap constraint is aggregated into the movement limit of each endpoint. The sum of compliance and fiber length is minimized by using the method of moving asymptotes (MMA) [74].

Unlike the orthotropic materials usually assumed in previous studies, the mechanical properties of the composites are analyzed by considering 11 representative hybrid elements consisting of truss members and

rectangular continuum elements. The coordinates of the nodes embedded in the truss elements were used as design variables to obtain continuous fiber paths, which MMA updated to minimize compliance and fiber length. In each iteration, the nodes can only be moved within an acceptable range to avoid numerical instability. This approach has several significant advantages. First, since the polylines represent fiber trajectories, fiber paths can be obtained directly without post-processing. Second, hybrid elements consisting of embedded trusses and continuum elements can better reflect the mechanical properties of fiber-reinforced composites. Third, using a small number of representative endpoints to control fiber paths can reduce design variables and improve optimization efficiency. In addition, the number of truss elements used to represent the fibers gradually increases. A smaller number of elements at the beginning can improve computational efficiency. In the final optimization stage, more truss elements can accurately represent the fiber paths and control the fiber spacing.

The paper is organized as follows. Section 2 describes the finite element analysis of VSC. The optimization problem and its sensitivity analysis are given in Section 3. Section 4 describes the numerical implementation. Numerical examples are demonstrated in Section 5. Finally, Section 6 concludes the article.

2. Finite element analysis of VSC

In some reinforced concrete studies, fiber-reinforced concrete is described as a hybrid element [75,76]. The fibers are discretized as multiple fiber segments, which are embedded truss elements; the meshes of the fibers are generated independently of the matrix material meshes. Moreover, a coupling procedure is used to connect the two independent meshes. In this work, we apply such methods to finite element analysis of VSCs. The schematic of three fibers (dashed lines) embedded in 4×4 rectangular elements is shown in Fig. 1.

Finite element analysis for the static elasticity problem of fiber-reinforced structures yields a linear system of equations,

$$\mathbf{K}\mathbf{u} - \mathbf{F} = 0 \quad (1)$$

where \mathbf{u} is the global displacement vector of the continuum element; \mathbf{F} is the global force vector; \mathbf{K} is the global stiffness matrix. For the quadrilateral isoparametric element with four nodes and eight degrees of freedom, its elemental stiffness matrix consists of two items as

$$\mathbf{K}_e = \mathbf{K}_r + \mathbf{K}_{con} \quad (2)$$

where \mathbf{K}_{con} is the stiffness matrix of the continuum element and the \mathbf{K}_r is the stiffness matrix of the embedded truss elements, given as

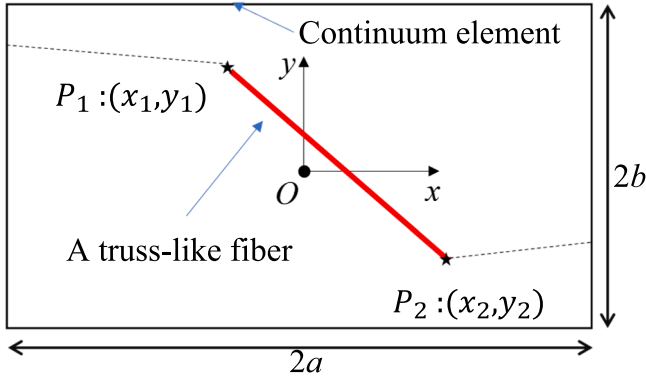


Fig. 2. The first hybrid element: the red lines represent the truss element embedded in the continuum element. Dashed lines indicate other fiber segments connected to it. The coordinates of two nodes, P_1 and P_2 , are (x_1, y_1) and (x_2, y_2) , respectively. a and b are half of the side length of the rectangular element.

$$\mathbf{K}_{tr} = \sum_{8 \times 8} \mathbf{K}_{tr_e} \quad (3)$$

where \mathbf{K}_{tr_e} is the stiffness matrix resulted from an individual truss element as shown in Fig. 2.

Usually, the stiffness matrix for a truss element is

$$\mathbf{K}_{tr}^* = \frac{AE}{L} \begin{bmatrix} \lambda^2 & \lambda\kappa & -\lambda^2 & -\lambda\kappa \\ \lambda\kappa & \kappa^2 & -\lambda\kappa & -\kappa^2 \\ -\lambda^2 & -\lambda\kappa & \lambda^2 & \lambda\kappa \\ -\lambda\kappa & -\kappa^2 & \lambda\kappa & \kappa^2 \end{bmatrix} \quad (4)$$

with A , E , and l being the truss element cross-sectional area, Young's modulus and length, respectively, and

$$\lambda = \frac{y_2 - y_1}{l}, \kappa = \frac{x_2 - x_1}{l} \quad (5)$$

where $x_1(x_2)$ and $y_1(y_2)$ are the coordinates of the truss nodes.

Consider the stiffness matrix of a continuum \mathbf{K}_{con} obtained by means of a finite element method and the stiffness matrix from a single embedded truss element \mathbf{K}^* . The challenge is to add the contribution of \mathbf{K}^* onto \mathbf{K}_{con} .

For the quadrilateral isoparametric element, the shape function is

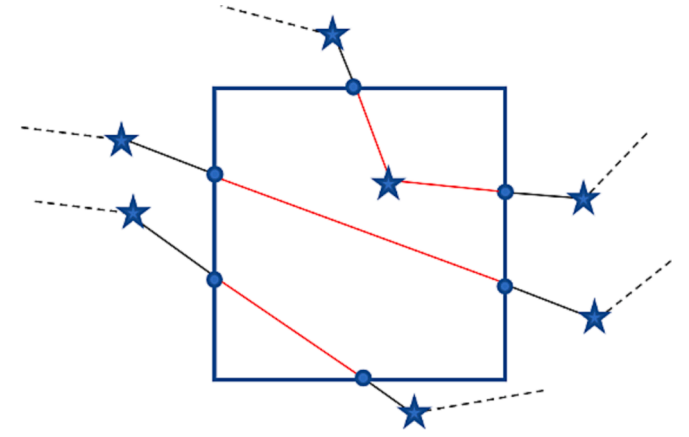


Fig. 4. An example of three discrete fiber segments in a representative hybrid element.

$$\begin{aligned} N_1(x, y) &= \frac{1}{4} \left(1 + \frac{x}{a}\right) \left(1 + \frac{y}{b}\right) \\ N_2(x, y) &= \frac{1}{4} \left(1 - \frac{x}{a}\right) \left(1 + \frac{y}{b}\right) \\ N_3(x, y) &= \frac{1}{4} \left(1 - \frac{x}{a}\right) \left(1 - \frac{y}{b}\right) \\ N_4(x, y) &= \frac{1}{4} \left(1 + \frac{x}{a}\right) \left(1 - \frac{y}{b}\right) \end{aligned} \quad (6)$$

Assuming that two nodes are inside the continuum element (Fig. 2), the node displacement vector of the truss can be calculated as

$$\mathbf{u}_{tr} = \begin{bmatrix} u_1 \\ v_1 \\ u_2 \\ v_2 \end{bmatrix} = \begin{bmatrix} N_1 & 0 & N_2 & 0 & N_3 & 0 & N_4 & 0 \\ 0 & N_1 & 0 & N_2 & 0 & N_3 & 0 & N_4 \\ N_1 & 0 & N_2 & 0 & N_3 & 0 & N_4 & 0 \\ 0 & N_1 & 0 & N_2 & 0 & N_3 & 0 & N_4 \end{bmatrix} \mathbf{u}_e = \mathbf{N} \mathbf{u}_e \quad (7)$$

The stiffness matrix of a single truss node \mathbf{K}^* will be mapped to another matrix \mathbf{K}_{tr} in terms of the continuum nodes, so that its contribution can be added to \mathbf{K}_{con} . Therefore, we have

$$\mathbf{N}^T \mathbf{K}^* \mathbf{N} = \mathbf{K}_{tr} \quad (8)$$

where \mathbf{N} is the transformation function matrix.

The above description only considers the case where discrete fiber segments are fully embedded in continuous elements. To sweep all possible intersection manners, 11 representative hybrid elements, as shown in Fig. 3, are considered in this work to achieve a complete material description. Note that the blue rectangles represent continuous elements, and the red and black line segments represent discrete fibers

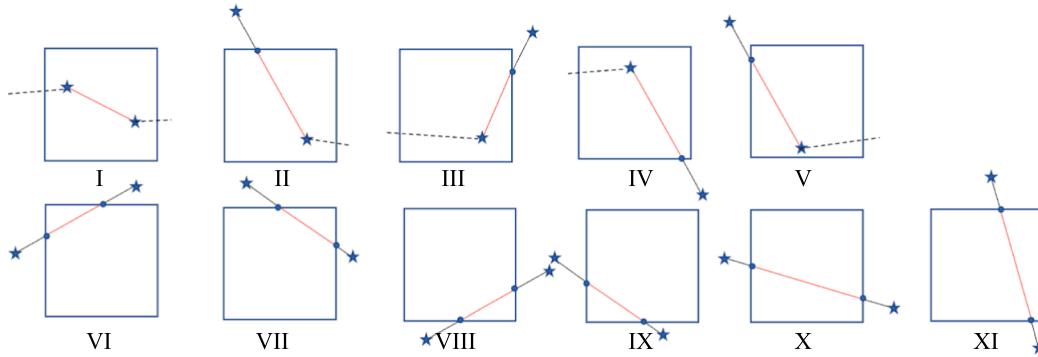


Fig. 3. The 11 representative hybrid elements considering all potential fiber-passing manners through the rectangular continuum element. The red line segment represents the part that contributes to the stiffness of the hybrid element, and the black line segment represents the part that is not inside the hybrid element and therefore does not contribute to the stiffness. Dashed lines indicate other connected fiber segments.

inside and outside the elements, respectively. The blue dots represent the intersections of the element boundaries with the discrete fiber segments. Star points denote nodes of discrete fiber segments whose coordinates are design variables. Only the fiber segments embedded inside the hybrid element contribute to the stiffness of that element. Therefore, in the case where a fiber segment has intersections with a hybrid element, the calculation of its stiffness matrix should replace the nodal coordinates (star nodes) with the corresponding intersection coordinates (blue dots). The coordinates of the intersection points C and D are calculated by linear interpolation, given as

$$\{x_C, x_D, y_C, y_D\} = f(x_1, x_2, y_1, y_2, a, b) \quad (9)$$

where function f is given in the Appendix for all hybrid elements.

There are cases where multiple discrete fibers are present in the same hybrid element (Fig. 4).

The stiffness of the hybrid element is provided by the matrix material and all the fiber segments embedded in the element; that is,

$$\mathbf{K}_e = \mathbf{K}_{con} + \sum_{i=1}^n \mathbf{K}_{ir,i} \quad (10)$$

where n is the number of fiber segments embedded in the element. For the case in Fig. 4, n should take 4.

3. Optimization problem and procedure

3.1. Problem formulation

Compliance is an essential criterion for performance in structural design evaluation. As such, it is used as the objective of this work. Similarly, optimization objectives have been widely adopted in related research on composite optimization [39]. Like volume fraction constraint, length constraint is used in fiber path design. In addition, such a constraint can avoid twisted fibers and fiber paths with sharp angles as it can effectively control the curvatures. Thus, the costing function in optimization is given as:

$$\begin{aligned} \text{find } \mathbf{x} &= \{x_1, x_2, \dots, x_M\} \\ \min f(\mathbf{x}, \mathbf{d}, \mathbf{u}) &= C \\ \text{s.t. } \mathbf{K}\mathbf{u} - \mathbf{F} &= 0 \\ L &< L_{\exp} \end{aligned} \quad (11)$$

The design variables \mathbf{x} are nodal coordinate vectors of M nodes. \mathbf{x}_k ($k = 1, 2, \dots, M$) is the coordinate vector of the k^{th} node with an unknown location in the matrix with M as the number of such nodes. L is the total length of the embedded truss, and L_{\exp} is the fiber length limit. The total compliance of an elastic body is

$$C = \mathbf{F}^T \mathbf{u} \quad (12)$$

According to the static equilibrium equation, $\mathbf{K}\mathbf{u} = \mathbf{F}$, Eq. (12) can be rewritten as

$$C = \mathbf{F}^T \mathbf{u} = \mathbf{u}^T \mathbf{K}^T \mathbf{u} \quad (13)$$

The discrete form corresponds to

$$C_e = \mathbf{F}_e^T \mathbf{u}_e = \mathbf{u}_e^T \mathbf{K}_e^T \mathbf{u}_e \quad (14)$$

where \mathbf{K}_e is the elemental stiffness matrix, and \mathbf{F}_e is the load applied on the element. According to the above equation, the total compliance is the sum of the compliance of all elements; that is,

$$C = \sum_{e=1}^n \mathbf{u}_e^T \mathbf{K}_e^T \mathbf{u}_e \quad (15)$$

where n is the number of the continuum element.

3.2. Sensitivity analysis

Because MMA is used to update the design variables, the first-order derivative of the costing function needs to be derived. The optimization problem subject to the elastic equation is equivalent to the minimization of a Lagrangian function, given as

$$\text{ming} = C + \lambda^T (\mathbf{K}\mathbf{u} - \mathbf{F}) \quad (16)$$

where λ is the Lagrange multiplier. To facilitate control of fiber spacing, nodes are only allowed to translate in the y -direction, although this operation may limit the design freedom of the fiber, which will be discussed in Section 5. Thus, the global sensitivity information should be the assembly of the sensitivity to one variable; that is

$$\mathbf{S} = \frac{\partial g}{\partial y_k} \quad (17)$$

It is necessary to solve the derivation of the Lagrange function to a design variable because it is necessary to find a stationary point; at that point, the derivation is equal to 0, given as

$$\frac{\partial g}{\partial y_k} = \frac{\partial C}{\partial y_k} + \lambda^T \frac{\partial (\mathbf{K}\mathbf{u} - \mathbf{F})}{\partial y_k} = 0 \quad (18)$$

The external loads are assumed to be independent of nodal coordinates, so the first-order derivation of the function is

$$\frac{\partial g}{\partial y_k} = \mathbf{F}^T \frac{\partial \mathbf{u}}{\partial y_k} + \lambda^T \left(\frac{\partial \mathbf{K}}{\partial y_k} \mathbf{u} + \mathbf{K} \frac{\partial \mathbf{u}}{\partial y_k} \right) \quad (19)$$

Rearranging the previous Eq. (15) leads to factoring out the derivation of the displacement

$$\frac{\partial g}{\partial y_k} = (\mathbf{F}^T + \lambda^T \mathbf{K}) \frac{\partial \mathbf{u}}{\partial y_k} + \lambda^T \frac{\partial \mathbf{K}}{\partial y_k} \mathbf{u} \quad (20)$$

The adjoint term should be equal to zero to remove the derivation of displacement, which means that our added unknown variable must satisfy

$$\lambda^T \mathbf{K} + \mathbf{F} = 0 \quad (21)$$

Thus

$$\frac{\partial g}{\partial y_k} = -\mathbf{u}^T \frac{\partial \mathbf{K}}{\partial y_k} \mathbf{u} \quad (22)$$

The derivative of g of the entire structure for y_k can be written as

$$\frac{\partial g}{\partial y_k} = \sum_{e=1}^n \mathbf{u}_e^T \frac{\partial \mathbf{K}_e}{\partial y_k} \mathbf{u}_e \quad (23)$$

and

$$\frac{\partial \mathbf{K}_e}{\partial y_k} = \frac{\partial \mathbf{K}_{con}}{\partial y_k} + \frac{\partial \mathbf{K}_{ir}}{\partial y_k} \quad (24)$$

The stiffness matrix of the continuum element is not related to the nodal coordinates of the truss element, so the first term is zero.

The derivative of the elemental stiffness with respect to the truss nodal position is

$$\frac{\partial \mathbf{K}_e}{\partial y_k} = \frac{\partial \mathbf{K}_e^+}{\partial y_k} = \frac{\partial \mathbf{N}^T}{\partial y_k} \mathbf{K}^* \mathbf{N} + \mathbf{N}^T \frac{\partial \mathbf{K}^*}{\partial y_k} \mathbf{N} + \mathbf{N}^T \mathbf{K}^* \frac{\partial \mathbf{N}}{\partial y_k} \quad (25)$$

In that manner, the global sensitivity becomes

$$\mathbf{S} = \sum_{e=1}^n -\mathbf{u}_e^T \frac{\partial \mathbf{N}^T}{\partial y_k} \mathbf{K}^* \mathbf{N} \mathbf{u}_e - \mathbf{u}_e^T \mathbf{N}^T \frac{\partial \mathbf{K}^*}{\partial y_k} \mathbf{N} \mathbf{u}_e - \mathbf{u}_e^T \mathbf{N}^T \mathbf{K}^* \frac{\partial \mathbf{N}}{\partial y_k} \mathbf{u}_e \quad (26)$$

Note that the power of y_k in \mathbf{N} is 1. Its second-order partial derivative is

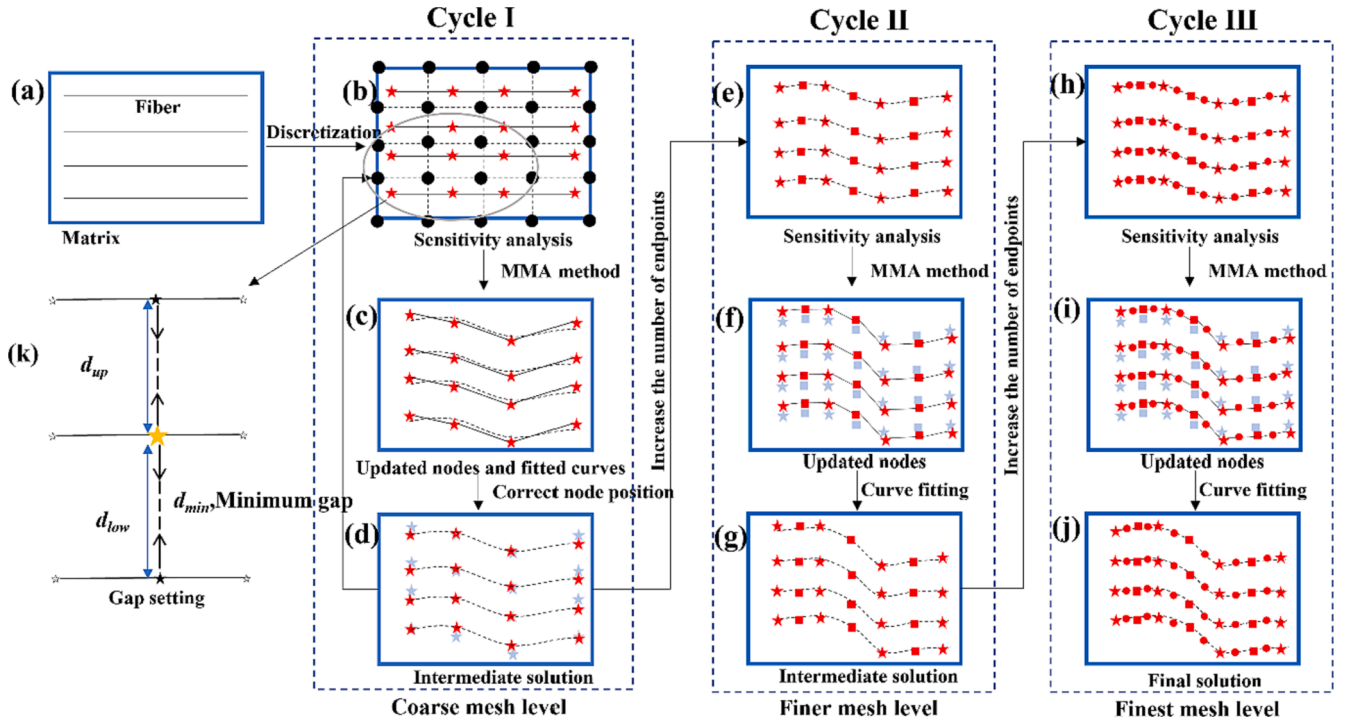


Fig. 5. The flowchart of a representative iteration in the method nodal-based fiber path optimization.

$$\frac{\partial S}{\partial y_k} = \sum_{e=1}^p \left(-u^T \frac{\partial N^T}{\partial y_k} \frac{\partial K^*}{\partial y_k} N u - u^T \frac{\partial N^T}{\partial y_k} K^* \frac{\partial K^*}{\partial y_k} u - u^T \frac{\partial N^T}{\partial y_k} \frac{\partial K^*}{\partial y_k} N u \right. \\ \left. - u^T N^T \frac{\partial^2 K^*}{\partial y_k^2} N u - u^T N^T \frac{\partial K^*}{\partial y_k} \frac{\partial N}{\partial y_k} u - u^T \frac{\partial N^T}{\partial y_k} K^* \frac{\partial N}{\partial y_k} u - u^T N^T \frac{\partial K^*}{\partial y_k} \frac{\partial N}{\partial y_k} u \right) \quad (27)$$

where p is the number of embedded trusses connecting node k . The total length is

$$L = \sum_{e=1}^{l \times q} L_e(x) \quad (28)$$

where L_e is the elemental length. The first and second derivatives of the total length are.

$$\frac{\partial L}{\partial y_k} = \frac{\partial \sum_{e=1}^{l \times q} L_e(x)}{\partial y_k} = \sum_{e=1}^{l \times q} \frac{\partial L_e(x)}{\partial y_k} \quad \text{and} \quad \frac{\partial^2 L}{\partial y_k^2} = \sum_{e=1}^{l \times q} \frac{\partial^2 L_e(x)}{\partial y_k^2} \quad (29)$$

4. Numerical implementation

4.1. Optimization procedure

The key idea of nodal-based fiber path optimization is using polylines to represent fibers. As shown in its flow chart in Fig. 5, each iteration contains four major steps: meshing, sensitivity analysis, nodal position updating, and nodal position correction. First, the dimensions and mechanical properties of the VSC to be optimized are input. The initial fibers in the horizontal direction are uniformly distributed inside the matrix, and the number of fibers is also determined (Fig. 5(a)). Then, this program meshes the matrix uniformly (dash lines) and picks a small number of nodes (red star nodes) on the fiber as the polyline endpoints (Fig. 5(b)). Afterward, the finite element analysis is performed to calculate the nodal displacement for sensitivity analysis in Eq. (1). The calculated sensitivities guide the MMA to upgrade the nodal coordinates.

Crossed fiber paths in composites facilitate load sharing, reducing stress concentrations and potential failure [48]. Crossings also enhance resistance to shear forces and promote interlocking between layers,

strengthening interlaminar shear strength and preventing delamination [77,78], contributing to a more durable material that can withstand various mechanical stresses. However, as previously mentioned, overlapped fibers fabricated by automated fiber placement or additive manufacturing lead to undesired thickness variations and even material failure. Therefore, in this work, which focuses solely on intersection-free fiber path optimization, controlling fiber spacing is crucial to ensure consistent thickness and prevent associated issues. In the implementation of MMA, the fiber nodes can only move in a prescribed range $[\alpha_{low}, \alpha_{up}]$ in the vertical direction to avoid fiber-crossing problems, which can be described as:

$$\alpha_{up} = \frac{d_{up} - d_{min}}{2}, \alpha_{low} = \frac{d_{low} - d_{min}}{2} \quad (30)$$

where d_{up}/d_{low} is the distance between a node (the yellow star in Fig. 5 (k)) on a fiber with the nearest node (the dark star) on its top/bottom adjacent fiber, and d_{min} represents the minimum manufacturable gap. With this scheme, the nodal coordinates are precisely controlled to avoid the problem of fiber crossings and overlaps.

However, the fibers connected by the optimized nodes are often not smooth (the solid line in Fig. 5(c)). The proposed method uses polynomial functions to fit the upgraded fiber nodes (dash line in Fig. 5(c)) to ensure smooth and continuous fibers. It moves the endpoints of the polyline to the fitted curve to correct the node positions (Fig. 5(d)). Like the previous upgrading node position, the nodes can only be shifted in the y -direction, and their x -coordinates remain unchanged. However, since the corrected node coordinates depend on the form of the fitted equation, the nodal position correction limits the range of movement of the node and reduces the design space. In order to avoid the fiber path being restricted to a specific area, we upgrade the node position every $Iter$ times and perform a correction of the node coordinates. In this work, $Iter = 10$. The above part is called Cycle I (Fig. 5). The convergence criterion of Cycle I optimization process is defined as

$$C_{err} = \frac{\left| \sum_{j=1}^3 |C_{k-j+1} - C_{k-3-j+1}| \right|}{\sum_{j=1}^3 C_{k-j+1}} \leq \delta_c \quad (31)$$

Table 1
Pseudocode of sensitivity analysis.

Algorithm 1 Sensitivity analysis	
Input: Symbolic expression of sensitivity dgx and dlx , truss element $elem$ of size $eln \times 2$, node coordinates $xval$ of size $2nn$, node displacement u	
Output: the sensitivities of the costing function $dfdx$ and $dhdxdx$ of size $2nn \times 1$	
1. Initialization the zero matrix $dfdx$ and $dhdxdx$ of size $2nn \times 1$	
2. for $n = 1$ to eln do	
3. $[x] \leftarrow nodalcoordinate (elem, xval, n)$	
4. $[p_1, p_2] \leftarrow nodenumber (elem, n)$	
5. $[a] \leftarrow intersectionpoint (p_1, p_2)$	
6. $[b_1, b_2, \dots, b_m] \leftarrow hybridelement (x)$	
7. For $j = 1$ to m do	
8. $[ue] \leftarrow nodaldisplacement (u, b_j)$	
9. $[Wj] \leftarrow \text{Evaluate the expression } dgx(x, a, ue)$	
10. $[Vj] \leftarrow \text{Evaluate the expression } dlx(p_1, p_2, a)$	
11. End	
12. $dfdx(p_1, p_2) \leftarrow dfdx(p_1, p_2) + \text{sum}(W)$	
13. $dhdxdx(p_1, p_2) \leftarrow dhdxdx(p_1, p_2) + \text{sum}(V)$	
14. END	

where C_{err} is the error of the compliance and the error limit, δ_c , is set as 1%.

However, the correction process often leads to intersections or too small spacings of the fitted paths. The finer mesh level represents fiber paths to control the nodal spacing between adjacent fibers. In Fig. 5(e), more nodes are inserted on the fitted fibers (The red square nodes). This operation has three advantages. First, the initial iterative process can use fewer nodes to reduce design variables and improve computational efficiency. Second, more nodes are more likely to exhibit smooth fiber paths. Third, a sufficient number of nodes ensures the spacing of fiber paths. When MMA upgrades nodal positions, the distances between fibers are gradually adjusted to meet the movement range constraints. In Fig. 5(g), the optimized nodal positions are also corrected by fitting the curve. The above steps are called Cycle II. Similarly, when the convergence condition is satisfied, the finest node level with more nodes is applied (Fig. 5(h)), which is Cycle III. This process will continue until the spacing of the fitted fiber paths meets manufacturing constraints.

4.2. Sensitivity assembling

Since the node positions of the fibers are constantly changing, the interpolation relationship shown in Eq. (9) is different, making it difficult to obtain an explicit objective function expression. Therefore, a concept similar to assembling a global stiffness matrix is used in the finite element analysis for sensitivity analysis. The sensitivity of Node 1 in Fig. 2 depends on the coordinates of itself and the affected nodes (Node 2). To calculate its sensitivity, as shown in the below pseudocode (Table 1),

After entering the material's properties, the hybrid element stiffness matrix is immediately assembled. Thus, the symbolic expression for the derivative of the design variables, dgx and dlx are also "pre-assembled" as explicit expressions in MATLAB. For simplicity purposes, this section uses first-order partial derivatives as an example, and the assembly process for second-order partial derivatives is consistent. After applying boundary conditions and finite element analysis, the displacement u of each continuum element's node can be calculated. The sensitivities of the nodal coordinates to the objective function and constraint equation are output in the matrix form $dfdx$ and $dhdxdx$, so the matrix size is consistent with truss nodal coordinates $xval$ (Table 1 Line 1). This algorithm calculates one by one in the order of embedded truss elements (Table 1 Line 2). The algorithm first extracts the truss nodal coordinates x (Table 1 Line 3) and the member node vector $[p_1, p_2]$ for the two nodes (Table 1 Line 4) of the n th truss element. The algorithm calculates the intersection coordinate vector, a , that this truss will produce with the mesh of the matrix material. In addition, the serial number of the corresponding continuum elements are also found, b_1, b_2, \dots, b_m (Table 1 Line

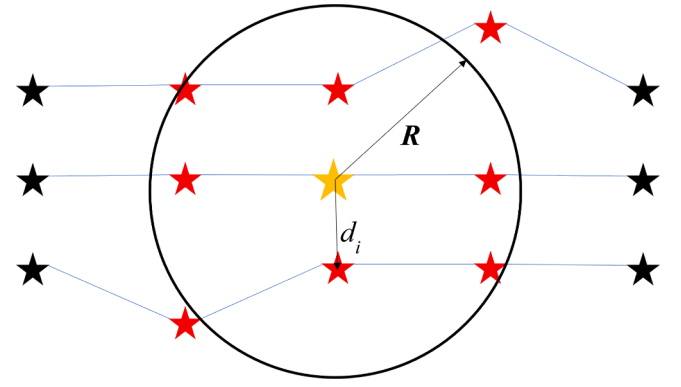


Fig. 6. The CSRBF filter: the red star nodes represent the nodes for the average filter.

6). Therefore, the truss element is divided into m subsections according to the number of continuum elements it passes through, and their contributions to the sensitivity are calculated one by one (Table 1 Line 7). The node displacement of the continuous element ue is found by the corresponding element serial number (Table 1 Line 8). Afterward, the corresponding elemental sensitivities matrix W_j and V_j of size 2×1 are calculated through the built-in *eval* function of MATLAB (Table 1 Lines 9 and 10). According to $[p_1, p_2]$, this elemental sensitivity matrix is assembled to the corresponding position of the sensitivity matrix $dfdx$ and $dhdxdx$ (Table 1 Lines 12 and 13). The algorithm will calculate the sensitivity of all elements. This "pre-assembled" explicit symbolic expression can significantly reduce repetitive calculations and improve computational efficiency.

4.3. Radial basis function-based filtering technique

To reduce excessive tortuosity in the fiber path and make the fiber path more concentrated, we introduce a filter based on the Radial basis function (RBF). There are many different RBFs, including Gaussian, Inverse Multiquadratic, Globally Supported Radial Basis Function, and Compact Supported Radial Basis Function (CSRBF) [79,80]. CSRBF has zero function values within a medium-sized support radius and typically consumes less memory for coefficient matrices and less computation for solving linear equations. In this work, CSRBF (weighting factor) with C^2 continuity is used:

$$\psi(r) = r_0^4(4r + 1) \quad (32)$$

where

$$r_0 = \max\{0, (1 - r)\} \quad (33)$$

$$r = \frac{d_i}{R} \quad (34)$$

where d_i is the distance between the support node and the i^{th} observation node, and R denotes the support radius. The yellow star node is the support node, and the circle with R as the radius represents the support range of this filter (Fig. 6). In this work, the R -value is set to the initial fiber spacing, g .

Therefore, the sensitivity of the i^{th} node should be

$$\bar{S}_i = \sum_{j=1}^q \psi_{ij} S_{ij} / \sum_{j=1}^q \psi_{ij} \quad (35)$$

where q is the node number in the support range of the filter.

As a comparison, an average-based filter algorithm is also introduced. The sensitivity of the i^{th} node is determined by itself and the surrounding nodes; that is,

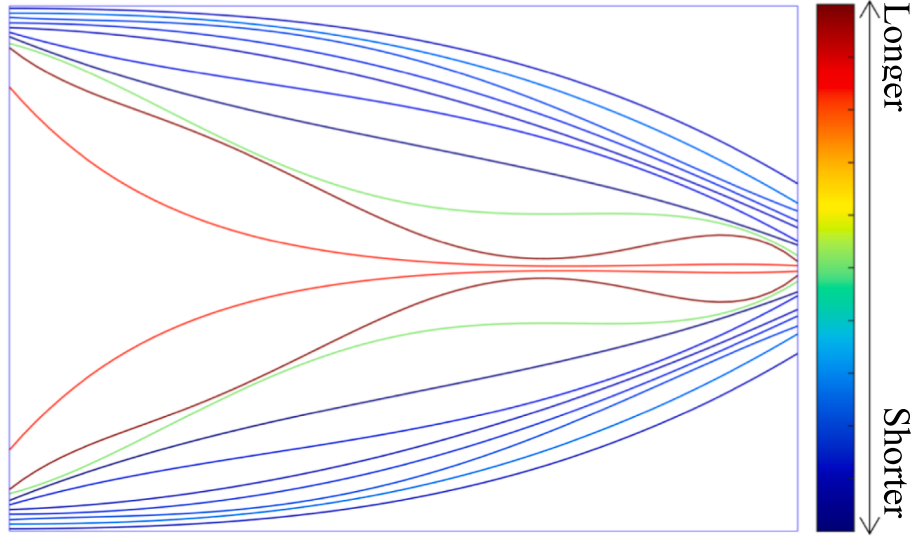


Fig. 7. The fiber distribution of the cantilever beam.

$$\bar{S}_i = \left(S_i + \sum_{j=1}^p S_j \right) / (p + 1) \quad (36)$$

where p is the number of the surrounding nodes. For example, the sensitivity of the yellow star node is determined by itself and its eight surrounding neighbors (the red node in Fig. 6).

4.4. Adaptive curve fitting

The updated polylines may have jagged structures that cannot represent smooth, continuous fibers. The proposed method uses an n^{th} ($n = 3, 4$, or 5) order polynomial to fit the curve (the dashed line in Fig. 5) and correct the node positions; that is,

$$y = \begin{cases} C_1x^5 + C_2x^4 + C_3x^3 + C_4x^2 + C_5x^1 + C_6 \\ C_2x^4 + C_3x^3 + C_4x^2 + C_5x^1 + C_6 \\ C_3x^3 + C_4x^2 + C_5x^1 + C_6 \end{cases} \quad (37)$$

where $C_1 \sim C_6$ are the coefficients to be fitted. The order of the fitting function is determined according to the fiber length.

Fig. 7 shows the fiber length distribution for the cantilever optimization case. Since fiber nodes are only allowed to translate in the y -direction, the more twisted the fiber, the longer its length. For longer and more tortuous fibers, this method uses a higher-order polynomial function to fit. For example, the indicated long green fibers in Fig. 7 were fitted with a 5th-order polynomial. The shorter red fibers were fitted with a 3rd-order polynomial. This process is called adaptive curve fitting. In this work, the proportions of the 5th, 4th and 3rd-order polynomials are 30%, 40%, and 30%, respectively.

5. Numerical examples

In this section, three examples of the design optimization of VSC are investigated to verify the effectiveness of the proposed method. Since the plane-stress state is assumed, these structures are subjected to in-plane loads. Furthermore, the thickness of VSC is set as 2, and the self-weight is not considered. In all the examples, the mechanical properties of the matrix material are $E_m = 1/15$ and $\nu_m = 0.3$, while the mechanical properties of the fiber are $E_f = 1$ and $\nu_f = 0.3$. In addition, the cross-sectional area of the fiber is $A_f = 1$. Fiber lengths are all limited to 110% of the original length.

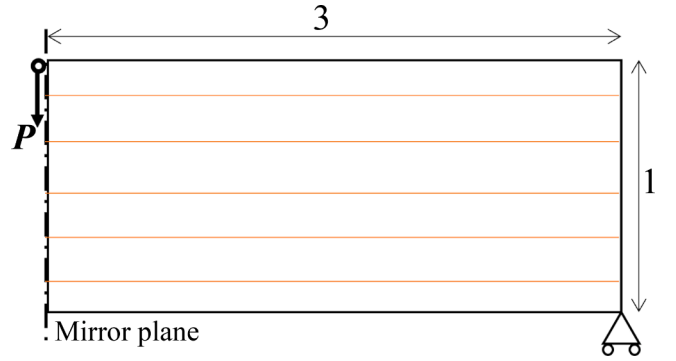


Fig. 8. Initial fibers in the MBB beam (right part).

5.1. MBB beam

The first example is to find the optimal distribution of fibers in a Messerschmitt–Bolkow–Blohm (MBB) with an aspect ratio of 3:1. Because of symmetry, only half structure is considered, and the nodes on the symmetry edge (dashed line in Fig. 8) only can move in the vertical direction. A downward force and a roller support are applied at the upper-left corner and the right-bottom corner, respectively. Without loss of generality, the initial fibers are straight lines uniformly distributed in the matrix. Note that the number of fibers is equivalent to the number of straight lines uniformly distributed in the initial structure (e.g., Fig. 8 shows five continuous long fibers).

The optimization results are shown in Fig. 9. During the optimization process, the upper right corner of the MMB hardly bears the load, so the fibers move slowly to the lower left. The fibers are mainly concentrated at the top and bottom of the MBB beam, and this distribution is very similar to the optimal structure of the MBB beam for isotropic material [81]. The fibers in the middle are longer, so higher-order polynomial functions are used for fitting, and there are multiple inflection points. This internal structure can also be observed in the optimal solution of the MBB beam. None of the final optimized fiber paths crossed, which complies with the manufacturing constraints. The convergence history is divided into three sections (Fig. 10) corresponding to Cycle I, II, and III. In Cycle I, compliance decreases to a minimum value. The curve fitting and correction process inevitably causes the nodes to deviate from the nodal positions obtained after MMA, leading to fluctuations in the

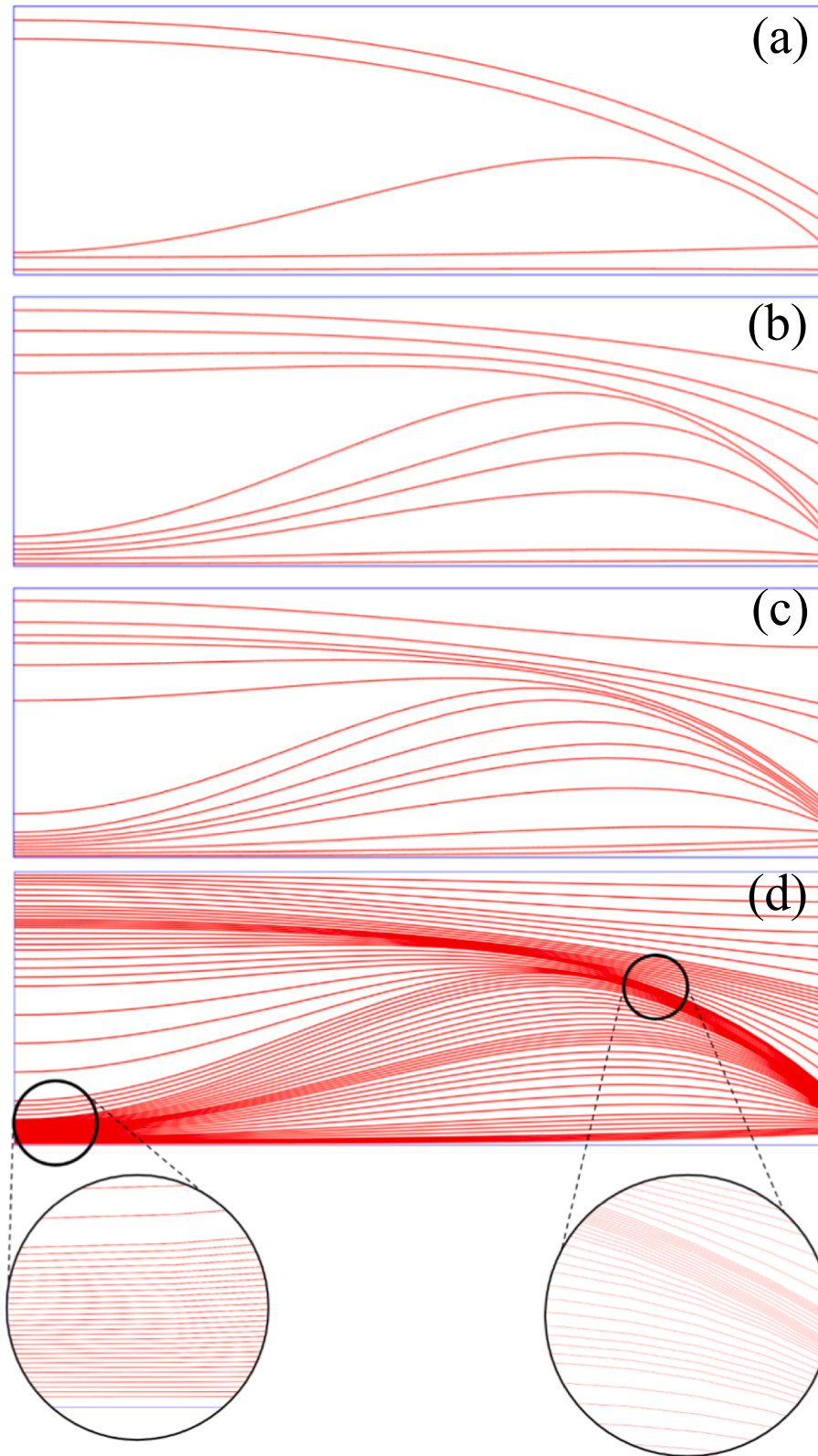


Fig. 9. Optimal fiber distribution in the MBB beam with n fibers: (a) $n = 5$, (b) $n = 10$, (c) $n = 15$, and (d) $n = 60$.

objective function. In Cycle II and III, the algorithm increased the optimal number of nodes and made the fiber spacing larger than the minimum manufacturable gap. Adopting more nodes results in slightly unstable convergence of the objective function but makes the fiber arrangement meet manufacturing requirements.

The normalized compliances (compliance/initial compliance) of 5-, 10-, 15-, and 60-fiber MBB beams are 0.4404, 0.5009, 0.4769, and 0.4566, respectively. The case in Fig. 9(d) also shows that the proposed method can be applied to the intensive case with many fibers, which is rare in other studies [39,82]. Local enlargements of the fiber densities

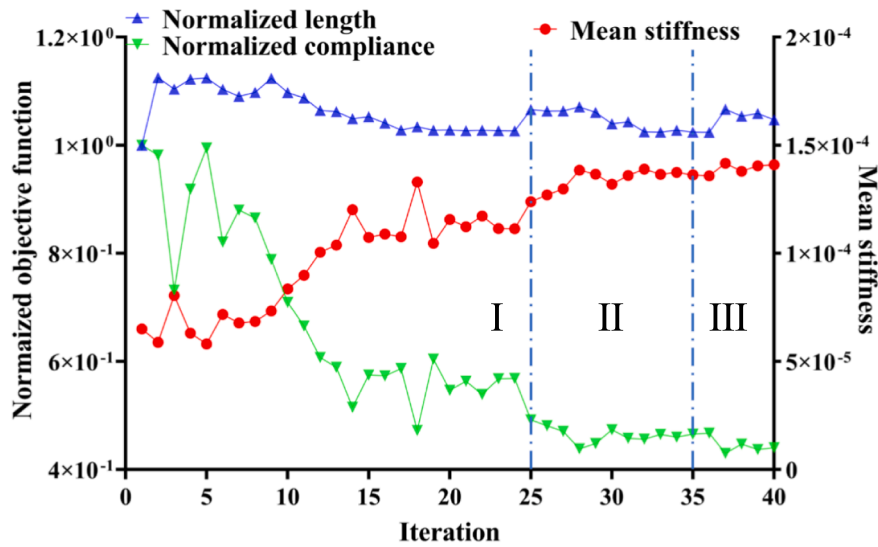
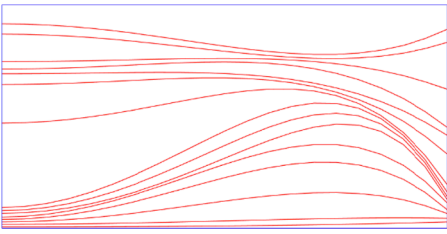
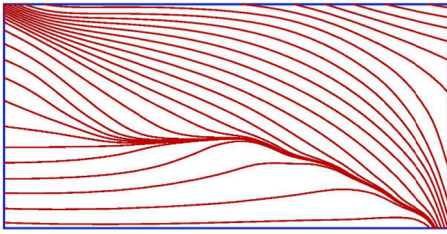


Fig. 10. The convergence history of MBB beam optimization with five fibers.

Table 2
Comparison of the MBB beam optimal results with an aspect ratio of 2:1.

Results	Compliance	Length	Mean stiffness	Iterations
	45.956	156.615	1.389×10^{-4}	40
	56.655	164.305	1.074×10^{-4}	27

are also given, without crossover or overlap problems. Additionally, the mean stiffness is introduced to study the efficiency of fiber; that is,

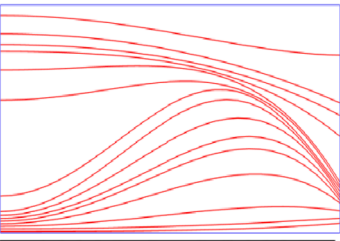
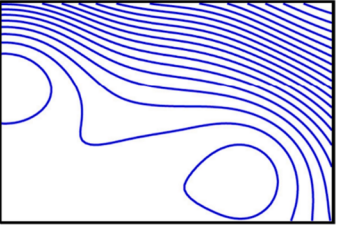
$$\bar{S} = \frac{1}{C \cdot L} \quad (38)$$

The mean stiffness of 5-, 10-, 15-, and 60-fiber MBB beam is 1.446×10^{-4} , 7.390×10^{-5} , 5.684×10^{-5} , and 5.4416×10^{-7} respectively, which means that as the number of fibers increases, the stiffness provided by the fibers per unit length decreases. However, in this study, the fiber nodes can only move in the y-direction, which limits the design space of the fiber path, and thus the compliance cannot be further reduced. This problem is significant in the case of more dense fibers. As shown in Fig. 9, the optimal fiber paths gradually become parallel and equally spaced with the increase of fiber number. The increase in the number of fibers limits the movement range of its nodes, making the decrease in compliance insignificant.

The right-hand sections of the MBB beams with aspect ratios of 2:1 and 3:2 are optimized for comparison (Table 2 and 3). There is no relevant optimization code for other optimization results in the

literature, and they tend to use finite element models for orthotropic materials. Therefore, this work performed finite element analysis by scanning their optimal fiber paths and inputting them into COMSOL using the physical properties parameters in this study. The results in Table 2 show that our optimization results in lower compliance with fewer fibers, and the higher mean stiffness also indicates that the structure obtained by this method is more efficient for utilizing fibers. Table 3 shows a 50%-56% decrease in compliance of the optimized MBB beam compared to the initial case. Thus, this one of their MBB examples does not impose fabrication constraints, so obvious fiber overlap and crossover problems can be seen. In another of their studies, the spacing range of fibers was further restricted so that the fiber paths remained essentially equally spaced. However, circular fiber paths emerged in their research, which is challenging to manufacture in practice [39]. Besides, their study uses a level set approach, which makes its iterations much more than the proposed method. In addition, their method uses orthogonal materials to characterize the composite properties, but the optimization results in many fiber-free regions, especially in the lower left corner. Therefore, the obtained fiber paths of this method depend on

Table 3
Comparison of the MBB beam optimal results with an aspect ratio of 3:2.

Results	Compliance	Length	Mean stiffness	Iterations
	38.533	141.984	1.827×10^{-4}	40
	32.157–47.980	129.128–145.762	$1.6141\text{--}2.267 \times 10^{-4}$	200–1000
Ref. [39]				

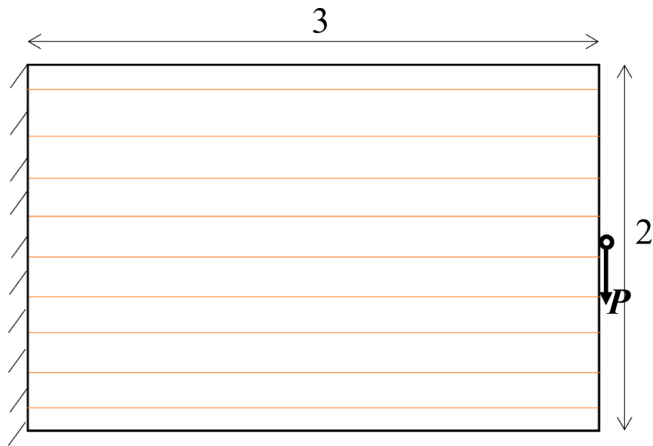


Fig. 11. Initial fibers in the cantilever beam.

the gradient vector of the level set function and may be inaccurate in the case of a small number of fibers.

5.2. Cantilever beam

The design optimization problem of a cantilever beam with an aspect ratio of 3:2 is shown in Fig. 11. The initial structure has horizontal fiber paths. Symmetry constraints are activated.

The optimization results are shown in Fig. 12(a). During the optimization process, the upper right corner and lower right corner of the cantilever beam hardly bear the load, so the fibers move slowly to the middle. The fibers at the right end are gradually concentrated towards the load point. This structure is also very close to the cantilever beam structure in continuum topology optimization [83]. None of the final optimized fiber paths crossed, complying with the manufacturing constraints.

Similarly, the convergence history is divided into three sections (Fig. 13). In Cycle I, the coarse mesh helps us quickly find an approximate result. In Cycles II and III, the method increased the density of the mesh, i.e., more nodes were used to represent fiber paths. As can be seen, compliance has risen slightly due to the need to adjust the fiber spacing to meet the manufacturing constraints. The cantilever beam with adaptive curve fitting has the lowest compliance, 0.2311.

The influence of the fitting function on the resulting fiber paths is also investigated. For comparison, the normalized compliances of the cantilever beams fitted by the 3rd, 4th and 5th order polynomials are 0.3576, 0.2337, and 0.2806, respectively. Too low order makes the fitting curve unable to describe more complex fiber paths, resulting in simple fiber paths and higher compliance (Fig. 12(b)). The fitting curves of higher-order polynomials can describe complex fiber paths and have less restriction on the design space, thus exhibiting better performance. However, too high order often makes the fitting overfit and creates some unnecessary structures appear. For example, some fibers at the right end of Fig. 12(d) are not concentrated at the load point.

Compared with the optimization result obtained from initial horizontal fibers, the optimization result for the initial configuration with vertical fibers (Fig. 14(a)) is different, although both gradually reveal the profile of the cantilever beam obtained by other optimization methods [83]. Fig. 14(b) and (c) show the fiber distribution at the 10th and 25th iterations. Although fiber paths remain discontinuous due to the coarse mesh in Cycles I and II, the paths roughly have the appearance of a cantilever beam. The fibers near the right end of the cantilever beam form a sharp angle, while the fibers in the middle show an almost network-like structure, which is a representative result of cantilever beam optimization. Fig. 14(d) shows the final optimal result with a mean stiffness of 1.637×10^{-4} . The same value in Fig. 12(a) is 2.901×10^{-4} . In addition, the initial value of mean stiffness with horizontal fibers (6.505×10^{-5}) is lower than that of vertical fibers (7.644×10^{-5}). Numerically, the optimized structure of horizontal fibers has a higher material utilization efficiency, but this conclusion varies from case to case. Furthermore, mono-direction-dominant fiber orientations, whether vertical or horizontal, throughout the optimization process indicates a dependency on the initial structure.

Similarly, a cantilever beam with a 3:1 aspect ratio was compared with results from other literature (Table 4). The fiber paths of cantilever beams were optimized using the level set method in related studies [38,39]. The results show that our results have shorter fiber lengths but lower compliance. The problem of equal spacing of fiber paths is considered in their studies and thus may further limit design freedom. In addition, the number of iterations of this proposed method is much lower than that of the level set-based method, and convergence results are obtained in only 30 iterations.

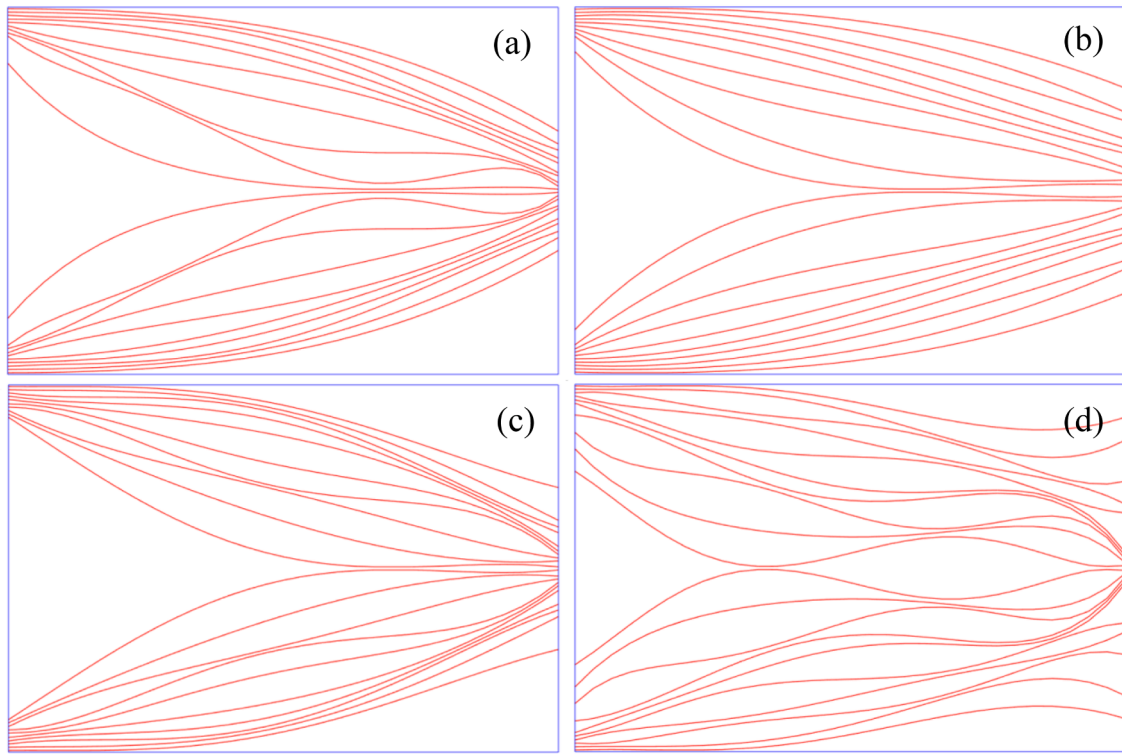


Fig. 12. Optimal fiber distributions in the cantilever beam with (a) the adaptive fitting function, (b) the 3rd-order polynomial, (c) the 4th-order polynomial, and (d) the 5th-order polynomial.

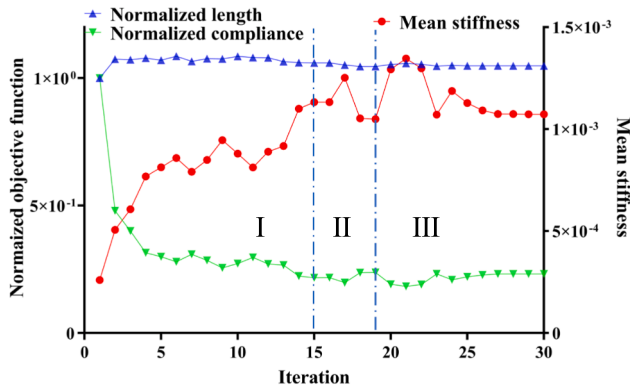


Fig. 13. The convergence history of the cantilever beam optimization with the adaptive curve fitting.

5.3. Bridge beam

The design optimization problem of a bridge-type beam is shown in Fig. 15. The design domain is a rectangle with an aspect ratio of 3:2, and the left edge and right bottom corners are fixed. Here, the structure has two concentrated forces. One force is applied at the left top corner, and another at the top edge middle point.

The influence of the filter on the resulting fiber paths is investigated. The optimization results using the RBF-based filter (Fig. 16(a)) have the lowest compliance (0.4361). The compliance of the optimized structure using the adjacent point average filter (Fig. 16(b)) and the filter-free optimized structure (Fig. 16(c)) is 0.4528 and 0.4028, respectively. Especially in the case without a filter, it can be seen that the fibers are distributed in the entire design domain, and there are still fibers in the upper right corner that cannot bear the load, which means that the

material is not fully utilized.

The effect of different filter radii on the optimization results is also studied. The compliances corresponding to the filter radius of $g/2$ (Fig. 17(a)) and $2g$ (Fig. 17(c)) are 0.4029 and 0.4570, respectively. The results are close to the optimization results without a filter (Fig. 17(c)) for the smaller filter radius, which means that the filter is too small to make the filter almost useless. For the larger filter radius, the sensitivity filter considers more nodes so that the fibers are over-concentrated, and fiber reinforcement is lost in some areas that require fiber support.

5.4. L-shaped bracket

The benchmarking of the L-shaped bracket has been less investigated in fiber optimization studies (Fig. 18). The top edge is fully fixed, and a concentrated downward force is applied to the top corner of the right end. For this case, a vertically aligned initial fiber configuration is used, and the x-coordinates of the fiber nodes are used as a design variable. In addition, the design domain of the L-shaped bracket is nonconvex, and the graph is divided into two sub-regions along the dotted line. The fibers are constrained in their initial sub-regions to avoid the problem of fibers going beyond the design domain.

Fig. 19 shows the optimization results with 15 and 30 fibers. The normalized compliances of 15- and 30-fiber L-shaped brackets are 0.2410 and 0.2552, respectively. The mean stiffness of the 15-fiber result is 6.413×10^{-5} , higher than the one of the 30-fiber (3.080×10^{-5}). Consistent with the previous MMB beam case, the fewer the fibers, the more fiber stiffness per unit length is provided.

Both optimal fiber distributions show a similar profile, found in other optimization studies on the L-shaped bracket [70,84,85], which shows a potential solution to the dependency on the initial structure using the region-dependent fiber initials. The lower left and lower right areas are less loaded and therefore have less fiber distribution. In Fig. 19(a), the fibers in the left half are divided into two bundles and distributed along the border, leaving a blank area in the middle. After adding more fibers

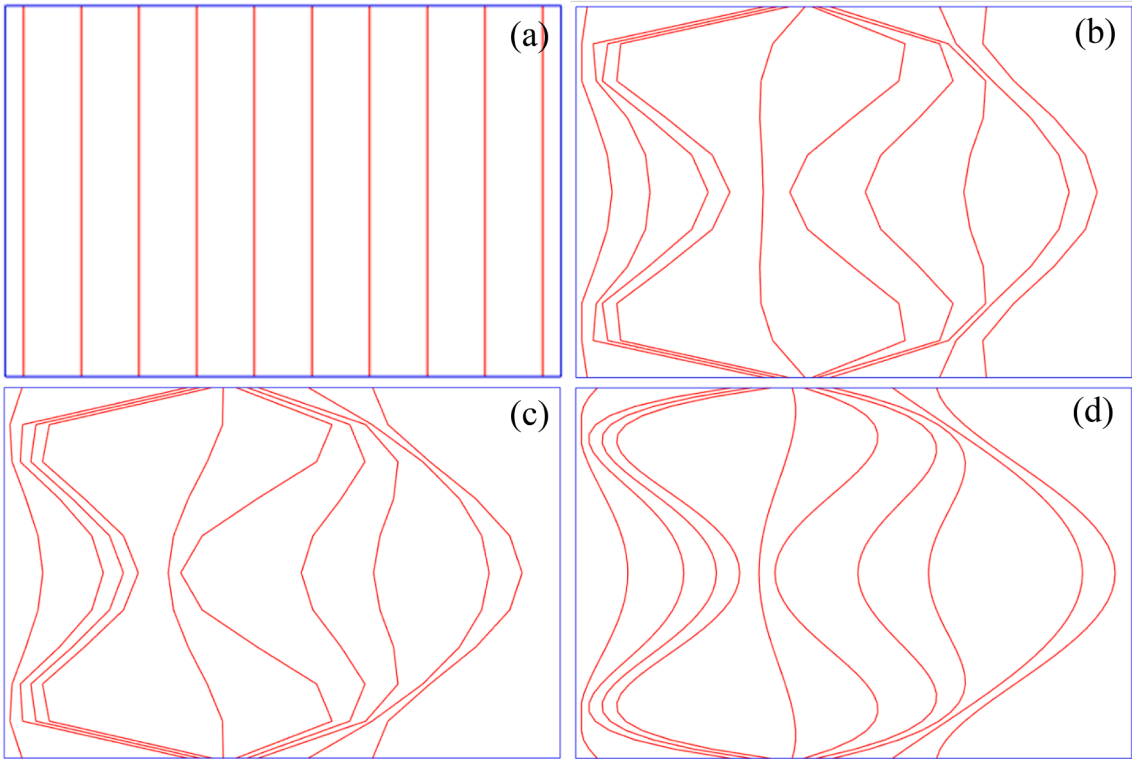
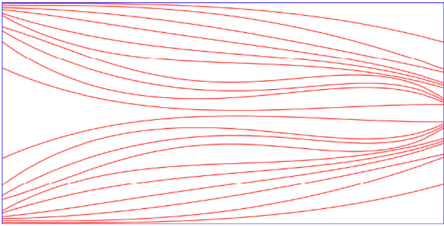
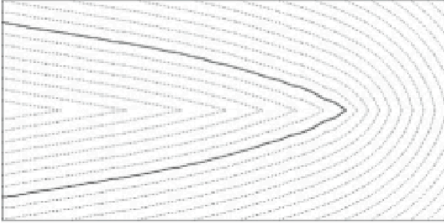
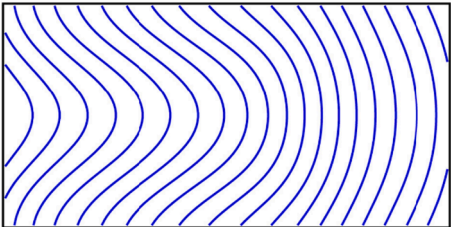


Fig. 14. The fiber distribution in a cantilever beam with initial vertical fibers at the iteration step (a) $m = 0$; (b) $m = 10$; (c) $m = 25$ and (d) $m = 40$.

Table 4
Comparison of the cantilever beam optimal results with an aspect ratio of 3:1.

Results	Compliance	Length	Mean stiffness	Iterations
	33.010	407.710	7.430×10^{-5}	30
	48.511	429.769	4.796×10^{-5}	900–1000
Ref. [38]				
	38.843	406.007	6.341×10^{-5}	600–700
Ref. [39]				

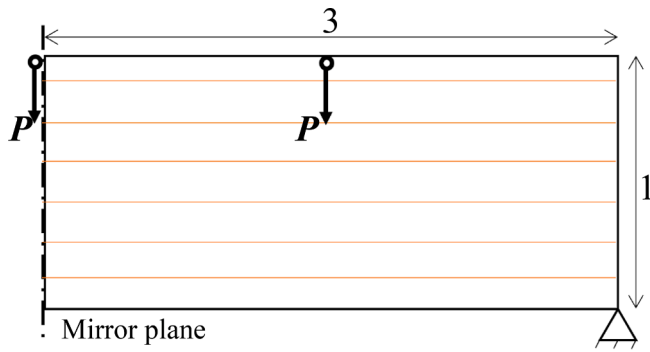


Fig. 15. Initial fibers in the bridge beam design problem.

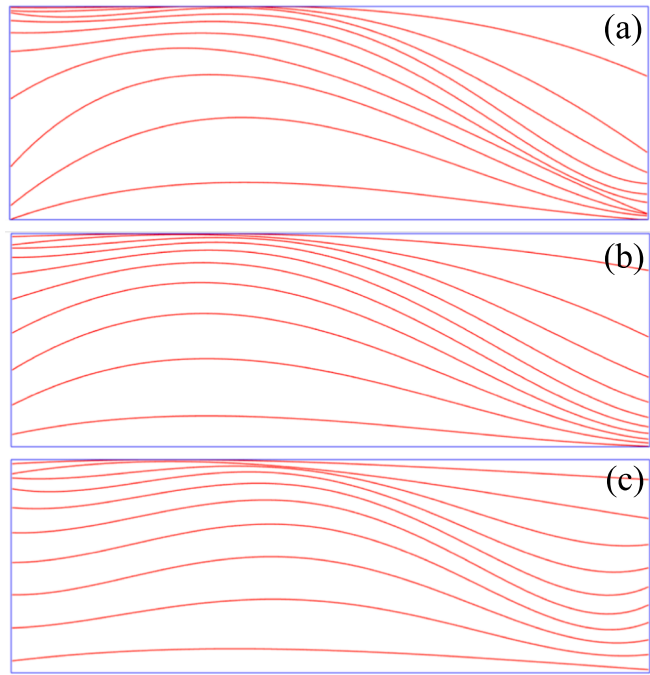


Fig. 16. Optimal fiber distribution in the bridge with different filtering techniques (a) with filter based on RBF; (b) with filter based on adjacent point average, and (c) non-filter.

(Fig. 19(b)), the original blank area is filled with several twisted fibers, and this form of structure can effectively improve the stiffness [70,84].

Although the above four examples obtained similar results in other literature, proving the validity of the proposed method, the proposed method still has some limitations. First, the final optimization results depend on the initial configuration. The approximate orientation of the fibers (vertical/horizontal) is determined in the initial setup, and a similar limitation was also discovered in the level-set method [38]. The second problem is that it limits the design space. Using the y-coordinates of the nodes as design variables limits the node movement, which is a compromise made to control the fiber spacing. In addition, the manufacturing constraints considered in this study are still inadequate. The nodal moving limit constrains the fibers' minimum spacing, but the maximum fabricable spacing [39] is not introduced. Due to the curve fitting, the fiber path does not show sharp corners. Our future research will focus on optimizing fiber-reinforced composites with multiple layers and curvature constraints on the fiber paths.

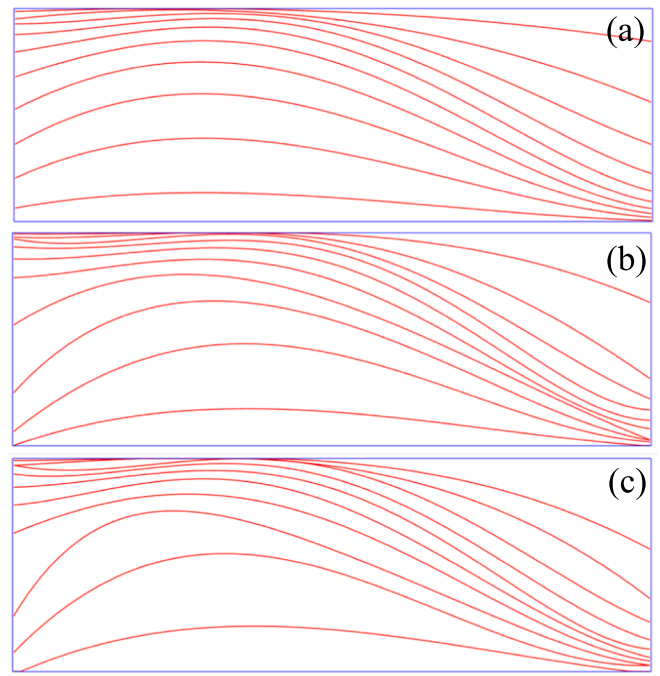


Fig. 17. Optimal fiber distribution in the bridge with different filter radii: (a) $R = g/2$; (b) $R = g$ and (c) $R = 2g$.

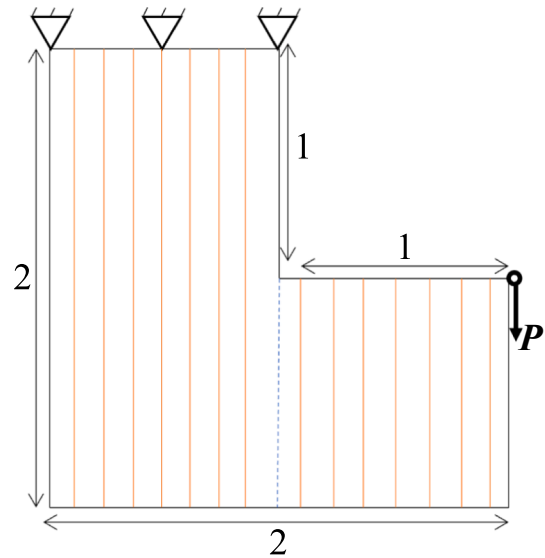


Fig. 18. Initial fibers in the L-shaped bracket design problem.

6. Conclusions

The adoption of fiber-reinforced structures has become imperative to increase the mechanical performance of structures. This paper assumes fiber paths in the matrix material as a truss network and minimizes compliance via moving truss nodes to optimal locations in the design domain. A finite element analysis method is proposed to simulate the deformation of fiber-reinforced structures by considering 11 representative hybrid elements with different truss intersection manners with the rectangular continuum element.

The nodal position appears in design variables for fiber path optimization for the first time. By controlling the movement range of the design variables in MMA, fiber crossing or overlapping problems are prevented. Thus, fiber smoothness and continuity are guaranteed

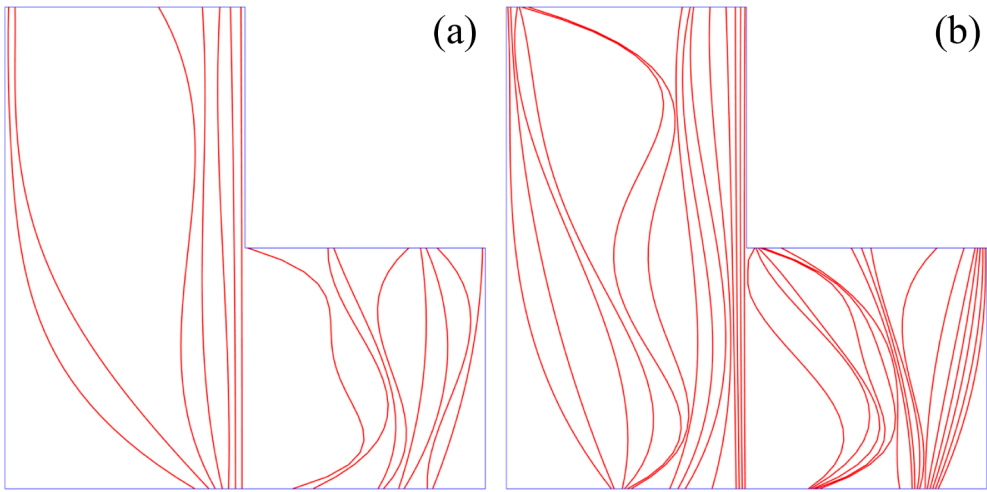


Fig. 19. Optimal fiber distribution in the L-shaped bracket with n fibers: (a) $n = 15$ and (b) $n = 30$.

Table A1
Comparison of maximum displacement of MATLAB and COMSOL.

Case	Schematic	$\delta_x/u_{c,x}$	$\delta_y/u_{c,y}$	δ_e/w_c
1		0.513%	1.231%	0.754%
2		0.117%	0.629%	0.442%
3		0.426%	1.152%	0.612%

through the adaptive curve fitting. In addition, this number of fiber nodes increases with iteration, improving the initial step efficiency and increasing the final result accuracy.

The proposed method can optimize the fiber paths and produce a manufacturable solution within 30 iterations in all cases examined. In the case of the most significant effect, compared to the initial cantilever beam, the methods can reduce compliance by approximately 77% with just a little fiber material increase (<10%). These results exceed or are at the same level as other fiber path optimization methods. However, the mono-axis design variables and fitting functions in the proposed optimization algorithm, although technically avoiding fiber crossings, limit the design freedom, which hinders the exploitation of VSC performance potential. Therefore, additional work, refining the method and adding appropriate constraints, is necessary to define fiber paths that can be manufactured using advanced fiber placement techniques.

CRediT authorship contribution statement

Xuyu Zhang: Investigation, Methodology, Software, Visualization, Writing – original draft. **Yi Min Xie:** Resources, Supervision, Writing – review & editing. **Qing Li:** Investigation, Writing – review & editing. **Cong Wang:** Investigation, Writing – review & editing. **Zicheng Zhuang:** Writing – review & editing. **He Li:** Writing – review & editing. **Shiwei Zhou:** Software, Conceptualization, Resources, Supervision, Writing – review & editing.

Declaration of Competing Interest

The authors declare that they have no known competing financial interests or personal relationships that could have appeared to influence the work reported in this paper.

Table A2
Hybrid element with no intersection.

Case	Schematic	Equation variant
1		$x_c = x_1;$ $y_c = y_1;$ $x_d = x_2;$ $y_d = y_2$

Table A3
Hybrid element with one intersection point.

Case	Schematic	Equation variant
2		$x_c = x_1 + \frac{(y_1 - b)(x_2 - x_1)}{(y_1 - y_2)};$ $y_c = b;$ $x_d = x_2;$ $y_d = y_2;$
3		$x_c = a;$ $y_c = y_2 + \frac{(a - x_2)(y_1 - y_2)}{(x_1 - x_2)};$ $x_d = x_2;$ $y_d = y_2;$
4		$x_c = x_2 + \frac{(y_2 + b)(x_1 - x_2)}{(y_2 - y_1)};$ $y_c = -b;$ $x_d = x_2;$ $y_d = y_2;$
5		$x_c = -a;$ $y_c = y_2 + \frac{(a + x_2)(y_1 - y_2)}{(x_2 - x_1)};$ $x_d = x_2;$ $y_d = y_2;$

Table A4
Hybrid element with two intersection points.

Case	Schematic	Equation variant
6		$x_c = x_1 + \frac{(y_1 - b)(x_2 - x_1)}{(y_1 - y_2)};$ $y_c = b;$ $x_d = -a;$ $y_d = y_2 - \frac{(a + x_2)(y_1 - y_2)}{(x_1 - x_2)};$
7		$x_c = x_1 + \frac{(y_1 - b)(x_2 - x_1)}{(y_1 - y_2)};$ $y_c = b;$ $x_d = a;$ $y_d = y_1 + \frac{(a - x_1)(y_2 - y_1)}{(x_2 - x_1)};$
8		$x_c = a;$ $y_c = y_2 + \frac{(a - x_2)(y_1 - y_2)}{(x_1 - x_2)};$ $x_d = x_1 + \frac{(y_1 + b)(x_2 - x_1)}{(y_1 - y_2)};$ $y_d = -b;$
9		$x_c = x_1 + \frac{(y_1 - b)(x_2 - x_1)}{(y_1 - y_2)};$ $y_c = b;$ $x_d = -a;$ $y_d = y_1 + \frac{(a + x_1)(y_2 - y_1)}{(x_1 - x_2)};$
10		$x_c = x_1 + \frac{(y_1 - b)(x_2 - x_1)}{(y_1 - y_2)};$ $y_c = b;$ $x_d = x_1 + \frac{(y_1 + b)(x_2 - x_1)}{(y_1 - y_2)};$ $y_d = -b;$
11		$x_c = -a;$ $y_c = y_2 + \frac{(a + x_2)(y_1 - y_2)}{(x_2 - x_1)};$ $x_d = x_2;$ $y_d = y_1 + \frac{(a - x_1)(y_2 - y_1)}{(x_2 - x_1)};$

Data availability

No data was used for the research described in the article.

Appendix A. Finite element verification

This work implemented numerical simulation in COMSOL to verify this finite element analysis method. The Young's moduli of the matrix and fiber materials are 1/15 and 1, respectively. The Poisson's ratio of the matrix material is 0.3, the thickness of the plate is 2, and the cross-sectional area of the fibers is 1.

The previous finite element analysis was coded in MATLAB. Moreover, the same plane stress model was modeled by COMSOL to compare the results. The validation work focuses on analyzing the displacement field distribution of the fibers. Comparing the displacement distribution over the fibers along the x-direction and y-direction, our previous finite element analysis and commercial software results are less different. Similarly, we also compare the strain energy (Table A1), the error of which is acceptable. In Table A1,

$\delta_x = |u_{m,x} - u_{c,x}|$, $\delta_y = |u_{m,y} - u_{c,y}|$, and $\delta_e = |w_m - w_c|$, (A.1) where $u_{m,x}$ and $u_{m,y}$ are the maximum displacements in the MATLAB model in x-direction, $u_{c,x}$ and $u_{c,y}$ are the maximum displacements in the COMSOL model in y-direction and w_m and w_c are the maximum elemental strain energy in MATLAB and COMSOL model.

Appendix B. Hybrid elements

The transformation matrix will change according to the positional relationship between the truss and the continuum element. Appendix B enumerates all possible cases and their Eq. (8) variation (shown in Tables A1–A4).

References

- [1] Goh GD, Yap YL, Agarwala S, Yeong WY. Recent progress in additive manufacturing of fiber reinforced polymer composite. *Adv Mater Technol* 2019;4: 1800271.
- [2] Fidan I, Imeri A, Gupta A, Hasanov S, Nasirov A, Elliott A, et al. The trends and challenges of fiber reinforced additive manufacturing. *Int J Adv Manuf Technol* 2019;102:1801–18.
- [3] Rajak DK, Pagar DD, Kumar R, Pruncu CI. Recent progress of reinforcement materials: a comprehensive overview of composite materials. *J Mater Res Technol* 2019;8:6354–74.
- [4] Prashanth S, Subbaya K, Nithin K, Sachchidananda S. Fiber reinforced composites-a review. *J Mater Sci Eng* 2017;6:2–6.
- [5] Mallick PK. Fiber-reinforced composites: materials, manufacturing, and design. CRC Press; 2007.
- [6] Xu Y, Zhu J, Wu Z, Cao Y, Zhao Y, Zhang W. A review on the design of laminated composite structures: constant and variable stiffness design and topology optimization. *Adv Compos Hybrid Mater* 2018;1:460–77.
- [7] Lozano GG, Tiwari A, Turner C, Astwood S. A review on design for manufacture of variable stiffness composite laminates. *Proc Inst Mech Eng B J Eng Manuf* 2016; 230:981–92.
- [8] Samukham S, Raju G, Vyasarayani C. Parametric instabilities of variable angle tow composite laminate under axial compression. *Compos Struct* 2017;166:229–38.
- [9] Zhu Y, Liu J, Liu D, Xu H, Yan C, Huang B, et al. Fiber path optimization based on a family of curves in composite laminate with a center hole. *Compos B Eng* 2017; 111:91–102.
- [10] Wu KC. Design and analysis of tow-steered composite shells using fiber placement. American society for composites 23rd annual technical conference; 2008.
- [11] Tosh M, Kelly D. On the design, manufacture and testing of trajectorial fibre steering for carbon fibre composite laminates. *Compos A Appl Sci Manuf* 2000;31: 1047–60.
- [12] Raju G, Wu Z, Kim BC, Weaver PM. Prebuckling and buckling analysis of variable angle tow plates with general boundary conditions. *Compos Struct* 2012;94: 2961–70.
- [13] Li H, Gao L, Li H, Li X, Tong H. Full-scale topology optimization for fiber-reinforced structures with continuous fiber paths. *Comput Methods Appl Mech Eng* 2021;377: 113668.
- [14] Diaz A, Bendsoe M. Shape optimization of structures for multiple loading conditions using a homogenization method. *Structural Optimization* 1992;4: 17–22.
- [15] Pedersen P. On thickness and orientational design with orthotropic materials. *Structural Optimization* 1991;3:69–78.
- [16] Pedersen P. On optimal orientation of orthotropic materials. *Structural Optimization* 1989;1:101–6.
- [17] Pedersen P. Bounds on elastic energy in solids of orthotropic materials. *Structural Optimization* 1990;2:55–63.
- [18] Olhoff N, Thomsen J, Rasmussen J. Topology optimization of bi-material structural structures. Elsevier Science Publisher BV; 1993.
- [19] Cheng H, Kikuchi N, Ma Z. An improved approach for determining the optimal orientation of orthotropic material. *Structural Optimization* 1994;8:101–12.
- [20] Luo J, Gea H. Optimal orientation of orthotropic materials using an energy based method. *Structural Optimization* 1998;15:230–6.
- [21] Papapetrou VS, Patel C, Tamijani AY. Stiffness-based optimization framework for the topology and fiber paths of continuous fiber composites. *Compos B Eng* 2020; 183:107681.
- [22] Yan X, Xu Q, Huang D, Zhong Y, Huang X. Concurrent topology design of structures and materials with optimal material orientation. *Compos Struct* 2019;220:473–80.
- [23] Sigmund O, Torquato S. Design of materials with extreme thermal expansion using a three-phase topology optimization method. *J Mech Phys Solids* 1997;45: 1037–67.
- [24] Stegmann J, Lund E. Discrete material optimization of general composite shell structures. *Int J Numer Meth Eng* 2005;62:2009–27.
- [25] Bruyneel M. SFP—a new parameterization based on shape functions for optimal material selection: application to conventional composite plies. *Struct Multidiscip Optim* 2011;43:17–27.
- [26] Gao T, Zhang W, Duysinx P. A bi-value coding parameterization scheme for the discrete optimal orientation design of the composite laminate. *Int J Numer Meth Eng* 2012;91:98–114.
- [27] Kiyono C, Silva E, Reddy J. A novel fiber optimization method based on normal distribution function with continuously varying fiber path. *Compos Struct* 2017; 160:503–15.
- [28] Ye M, Gao L, Li H. A design framework for gradually stiffer mechanical metamaterial induced by negative Poisson's ratio property. *Mater Des* 2020;192: 108751.
- [29] Luo Y, Li Q, Liu S. Topology optimization of shell-infill structures using an erosion-based interface identification method. *Comput Methods Appl Mech Eng* 2019;355: 94–112.
- [30] Kim D, Lee J, Nomura T, Dede EM, Yoo J, Min S. Topology optimization of functionally graded anisotropic composite structures using homogenization design method. *Comput Methods Appl Mech Eng* 2020;369:113220.
- [31] Bendsoe MP, Sigmund O. Topology optimization: theory, methods, and applications. Springer Science & Business Media; 2003.
- [32] Rozvany GI, Zhou M, Birker T. Generalized shape optimization without homogenization. *Structural optimization* 1992;4:250–2.
- [33] Bendsoe MP. Optimal shape design as a material distribution problem. *Structural Optimization* 1989;1:193–202.
- [34] Safonov AA. 3D topology optimization of continuous fiber-reinforced structures via natural evolution method. *Compos Struct* 2019;215:289–97.
- [35] Jiang D, Hoglund R, Smith DE. Continuous fiber angle topology optimization for polymer composite deposition additive manufacturing applications. *Fibers* 2019;7: 14.
- [36] Wang C, Xie YM, Lin X, Zhou S. A reaction diffusion-based B-spline level set (RDBLS) method for structural topology optimization. *Comput Methods Appl Mech Eng* 2022;398:115252.
- [37] Wang MY, Wang X, Guo D. A level set method for structural topology optimization. *Comput Methods Appl Mech Eng* 2003;192:227–46.
- [38] Brampton CJ, Wu KC, Kim HA. New optimization method for steered fiber composites using the level set method. *Struct Multidiscip Optim* 2015;52:493–505.
- [39] Tian Y, Shi T, Xia Q. A parametric level set method for the optimization of composite structures with curvilinear fibers. *Comput Methods Appl Mech Eng* 2022;388:114236.
- [40] Xu Y, Gao Y, Wu C, Fang J, Sun G, Steven GP, et al. Concurrent optimization of topological configuration and continuous fiber path for composite structures—A unified level set approach. *Comput Methods Appl Mech Eng* 2022;399:115350.

- [41] Huang X, Xie YM. Bi-directional evolutionary topology optimization of continuum structures with one or multiple materials. *Comput Mech* 2009;43:393–401.
- [42] Sun X, Yang J, Xie YM, Huang X, Zuo Z. Topology optimization of composite structure using bi-directional evolutionary structural optimization method. *Procedia Eng* 2011;14:2980–5.
- [43] Yan X, Huang X, Sun G, Xie YM. Two-scale optimal design of structures with thermal insulation materials. *Compos Struct* 2015;120:358–65.
- [44] Huang X, Zhou S, Sun G, Li G, Xie YM. Topology optimization for microstructures of viscoelastic composite materials. *Comput Methods Appl Mech Eng* 2015;283: 503–16.
- [45] Eckrich M, Arrabiyeh PA, Dlugaj AM, May D. Structural topology optimization and path planning for composites manufactured by fiber placement technologies. *Compos Struct* 2022;289:115488.
- [46] Brooks H, Molony S. Design and evaluation of additively manufactured parts with three dimensional continuous fibre reinforcement. *Mater Des* 2016;90:276–83.
- [47] Aragh BS, Farahani EB, Xu B, Ghasemnejad H, Mansur W. Manufacturable insight into modelling and design considerations in fibre-steered composite laminates: State of the art and perspective. *Comput Methods Appl Mech Eng* 2021;379: 113752.
- [48] Hasan KF, Horváth PG, Alpár T. Potential fabric-reinforced composites: a comprehensive review. *J Mater Sci* 2021;56:14381–415.
- [49] Nguyen MH, Vijayachandran AA, Davidson P, Call D, Lee D, Waas AM. Effect of automated fiber placement (AFP) manufacturing signature on mechanical performance of composite structures. *Compos Struct* 2019;228:111335.
- [50] Del Rossi D, Cadran V, Thakur P, Palardy-Sim M, Lapalme M, Lessard L. Experimental investigation of the effect of half gap/half overlap defects on the strength of composite structures fabricated using automated fibre placement (AFP). *Compos A Appl Sci Manuf* 2021;150:106610.
- [51] Woigk W, Hallett SR, Jones MI, Kuhtz M, Hornig A, Gude M. Experimental investigation of the effect of defects in Automated Fibre Placement produced composite laminates. *Compos Struct* 2018;201:1004–17.
- [52] Mishra V, Peeters DM, Abdalla MM. Stiffness and buckling analysis of variable stiffness laminates including the effect of automated fibre placement defects. *Compos Struct* 2019;226:111233.
- [53] Kim BC, Potter K, Weaver PM. Continuous tow shearing for manufacturing variable angle tow composites. *Compos A Appl Sci Manuf* 2012;43:1347–56.
- [54] Hine PJ, Lusti HR, Gusev AA. Numerical simulation of the effects of volume fraction, aspect ratio and fibre length distribution on the elastic and thermoelastic properties of short fibre composites. *Compos Sci Technol* 2002;62:1445–53.
- [55] Huang J, Haftka R. Optimization of fiber orientations near a hole for increased load-carrying capacity of composite laminates. *Struct Multidiscip Optim* 2005;30: 335–41.
- [56] Gürdal Z, Tatting BF, Wu C. Variable stiffness composite panels: effects of stiffness variation on the in-plane and buckling response. *Compos A Appl Sci Manuf* 2008; 39:911–22.
- [57] Muc A, Ulatowska A. Design of plates with curved fibre format. *Compos Struct* 2010;92:1728–33.
- [58] Blom AW, Tatting BF, Hol JM, Gürdal Z. Fiber path definitions for elastically tailored conical shells. *Compos B Eng* 2009;40:77–84.
- [59] Parnas L, Oral S, Ceyhan Ü. Optimum design of composite structures with curved fiber courses. *Compos Sci Technol* 2003;63:1071–82.
- [60] Wu Z, Raju G, Weaver PM. Framework for the buckling optimization of variable-angle tow composite plates. *AIAA J* 2015;53:3788–804.
- [61] Wu Z, Weaver PM, Raju G, Kim BC. Buckling analysis and optimisation of variable angle tow composite plates. *Thin-Walled Struct* 2012;60:163–72.
- [62] Hao P, Yuan X, Liu C, Wang B, Liu H, Li G, et al. An integrated framework of exact modeling, isogeometric analysis and optimization for variable-stiffness composite panels. *Comput Methods Appl Mech Eng* 2018;339:205–38.
- [63] Guo X, Zhang W, Zhong W. Doing topology optimization explicitly and geometrically—a new moving morphable components based framework. *J Appl Mech* 2014;81.
- [64] Sun Z, Song Z, Song J, Li H. Structural Optimization of Fiber-Reinforced Material Based on Moving Morphable Components (MMCs). *Acta Mech Solida Sin* 2022;35: 632–46.
- [65] Norato J, Bell B, Tortorelli DA. A geometry projection method for continuum-based topology optimization with discrete elements. *Comput Methods Appl Mech Eng* 2015;293:306–27.
- [66] Smith HA, Norato JA. Geometric constraints for the topology optimization of structures made of primitives. *SAMPE 2019-Charlotte, NC, May 2019; 2019*.
- [67] Smith H, Norato JA. Topology optimization with discrete geometric components made of composite materials. *Comput Methods Appl Mech Eng* 2021;376:113582.
- [68] Smith H, Norato J. Simultaneous material and topology optimization of composite laminates. *Comput Methods Appl Mech Eng* 2023;404:115781.
- [69] Xia Q, Shi T. Optimization of composite structures with continuous spatial variation of fiber angle through Shepard interpolation. *Compos Struct* 2017;182: 273–82.
- [70] Zhang X, Xie YM, Zhou S. A nodal-based evolutionary optimization algorithm for frame structures. *Comput Aided Civ Inf Eng* 2022.
- [71] Wang H, Chen Z, Wen G, Ji G, Xie YM. A robust node-shifting method for shape optimization of irregular gridshell structures. *Structures* Elsevier; 2021. p. 666–77.
- [72] Ding C, Seifi H, Dong S, Xie YM. A new node-shifting method for shape optimization of reticulated spatial structures. *Eng Struct* 2017;152:727–35.
- [73] Amir O, Sigmund O. Reinforcement layout design for concrete structures based on continuum damage and truss topology optimization. *Struct Multidiscip Optim* 2013;47:157–74.
- [74] Svanberg K. The method of moving asymptotes—a new method for structural optimization. *Int J Numer Meth Eng* 1987;24:359–73.
- [75] Bitencourt Jr LA, Manzoli OL, Bittencourt TN, Vecchio FJ. Numerical modeling of steel fiber reinforced concrete with a discrete and explicit representation of steel fibers. *Int J Solids Struct* 2019;159:171–90.
- [76] Zegard T, Paulino GH. Truss layout optimization within a continuum. *Struct Multidiscip Optim* 2013;48:1–16.
- [77] Kashani MH, Hosseini A, Sassani F, Ko F, Milani A. Understanding different types of coupling in mechanical behavior of woven fabric reinforcements: A critical review and analysis. *Compos Struct* 2017;179:558–67.
- [78] Zhou W, Wentz T, Liu D, Mao X, Zeng D, Torab H, et al. A comparative study of a quasi 3D woven composite with UD and 2D woven laminates. *Compos A Appl Sci Manuf* 2020;139:106139.
- [79] Wang S, Wang MY. Radial basis functions and level set method for structural topology optimization. *Int J Numer Meth Eng* 2006;65:2060–90.
- [80] Wei P, Li Z, Li X, Wang MY. An 88-line MATLAB code for the parameterized level set method based topology optimization using radial basis functions. *Struct Multidiscip Optim* 2018;58:831–49.
- [81] Andreassen E, Clausen A, Schevenels M, Lazarov BS, Sigmund O. Efficient topology optimization in MATLAB using 88 lines of code. *Struct Multidiscip Optim* 2011;43: 1–16.
- [82] Tian Y, Pu S, Zong Z, Shi T, Xia Q. Optimization of variable stiffness laminates with gap-overlap and curvature constraints. *Compos Struct* 2019;230:111494.
- [83] Fernandes RR, van de Werken N, Koirala P, Yap T, Tamijani AY, Tehrani M. Experimental investigation of additively manufactured continuous fiber reinforced composite parts with optimized topology and fiber paths. *Addit Manuf* 2021;44: 102056.
- [84] Lewiński T, Rozvany G. Exact analytical solutions for some popular benchmark problems in topology optimization III: L-shaped domains. *Struct Multidiscip Optim* 2008;35:165–74.
- [85] Kang Z, Wang Y, Wang Y. Structural topology optimization with minimum distance control of multiphase embedded components by level set method. *Comput Methods Appl Mech Eng* 2016;306:299–318.